THESIS

DISTORTIONS TO CURRENT-VOLTAGE CURVES OF CIGS CELLS WITH SPUTTERED Zn(O,S) BUFFER LAYERS

Submitted by

Tao Song

Department of Physics

In partial fulfillment of the requirements

For the Degree of Master of Science

Colorado State University

Fort Collins, Colorado

Fall 2013

Master's Committee:

Advisor: James R. Sites

Mingzhong Wu
Walajabad Sampath

ABSTRACT

DISTORTIONS TO CURRENT-VOLTAGE CURVES OF CIGS CELLS WITH SPUTTERED Zn(O,S) BUFFER LAYERS

Sputtered-deposited Zn(O,S) is an attractive alternative to CdS for $\mathrm{Cu(In,Ga)Se_2}$ (CIGS) thin-film solar cells' buffer layer. It has a higher band gap and thus allows greater blue photon collection to achieve higher photon current. The primary goal of the thesis is to investigate the effects of the secondary barrier at the buffer-absorber interface on the distortions to current-voltage (J-V) curves of sputtered-Zn(O,S)/CIGS solar cells. A straightforward photodiode model is employed in the numerical simulation to explain the physical mechanisms of the experimental J-V distortions including J-V crossover and red kink.

It is shown that the secondary barrier is influenced by both the internal material properties, such as the conduction-band offset (CBO) and the doping density of Zn(O,S), and the external conditions, such as the light intensity and operating temperature. A key parameter for the sputter deposition of Zn(O,S) has been the oxygen fraction in the argon beam. It is found that the CBO varies with the oxygen fraction in the argon beam at a fixed temperature. With a greater CBO ($\Delta E_C > 0.3\ eV$), the resulting energy barrier limits the electron current flowing across the interface and thus leads to the J-V distortion. Two different ZnS targets, non-indium and indium-doped one, were used to deposit the Zn(O,S) buffer layer. At the same oxygen fraction in argon beam, a non-In-doped Zn(O,S) buffer with a smaller amount of doping forms a greater secondary barrier to limit the electron current due to the compensation of the Zn(O,S) buffer layer. In addition, the temperature-dependent J-V crossover can be explained by the temperature-dependent impact of the secondary barrier – at lower temperature in the dark, the maximum

distortion-free barrier is reduced and results in a more serious current limitation, indicating a greater J-V crossover. It is also found that, under low-intensity illumination, there is a lower doping density of Zn(O,S) due to a smaller amount of photons with $h\nu > E_{g(Zn(O,S))}$ which can excite the buffer layer to release the trapped electrons from the deep-level defect state. The result is a greater secondary barrier to limit the electron current through the interface and shift the light J-V curve right towards the dark J-V curve at high bias $(V > V_{OC})$ which reduces the J-V crossover. Finally, the quantitative comparison of J-V distortion between simulation and experiment is employed to examine the credibility of the secondary barrier theory.

ACKNOWLEDGEMENTS

First, I would owe my sincere gratitude to my advisor Jim. Without your friendly reply when I was applying to graduate school, I would miss a knowledgeable advisor in PV research. Thank you for letting me do independent work and supporting me to attend conferences. My thesis would never be done without your patient and insightful guidance. I will never forget how pleasant I work with you over the two years.

Thanks to all the nice colleagues in the PV lab. I really appreciate Tyler for being a strong partner in the CIGS team, and Russell for showing me the solar cells characterization, and John, Jen, and Andy, for being friendly to me. Especially, Katherine, she was always warm-hearted whenever I asked for help. In addition, I am grateful to the CIGS team led by Kannan Ramanathan at NREL for providing the CIGS cells, and my committee members, Mingzhong Wu and Walajabad Sampath. The simulation software “wxAMPS” was designed at University of Illinois at Urbana-Champaign by Yiming Liu et al, following the physical principles of “AMPS” software developed at Pennsylvania State University by S. Fonash et al.

I am also very grateful to have a great time with Guhan, Serena, and other members in the Fort Collins Badminton Club. It was very kind of Houcheng for discussing with me whenever there was a tough course assignment and Zihui and Yiyan, for letting me feel comfortable at the first time I arrived at CSU.

To my beloved Ying, despite of a long distance between us, you were always here for me whenever I was down along these years. It is an amazing fortune to have you in my life.

Finally, I would owe my deepest thanks to my parents, Yufei Song and Qiaoe’ Zhang, and my younger brother, Chao Song. It is your endless love and support from the other side of the earth that encourages me to complete my degree.

TABLE OF CONTENTS

LIST OF FIGURES

LIST OF TABLES

Chapter 1

Introduction

1.1 Present Status and Prospective of Photovoltaics Energy

Currently the average worldwide energy consumption is approximately 15 TW, the majority of which is generated by the combustion of fossil fuels [1]. The associated CO_2 release from the burning of these fossil fuels is a primary cause of the climate change and global warming. In response to the goal of carbon-free power, many countries are driving increasing renewable energy legislation, incentives, and commercialization.

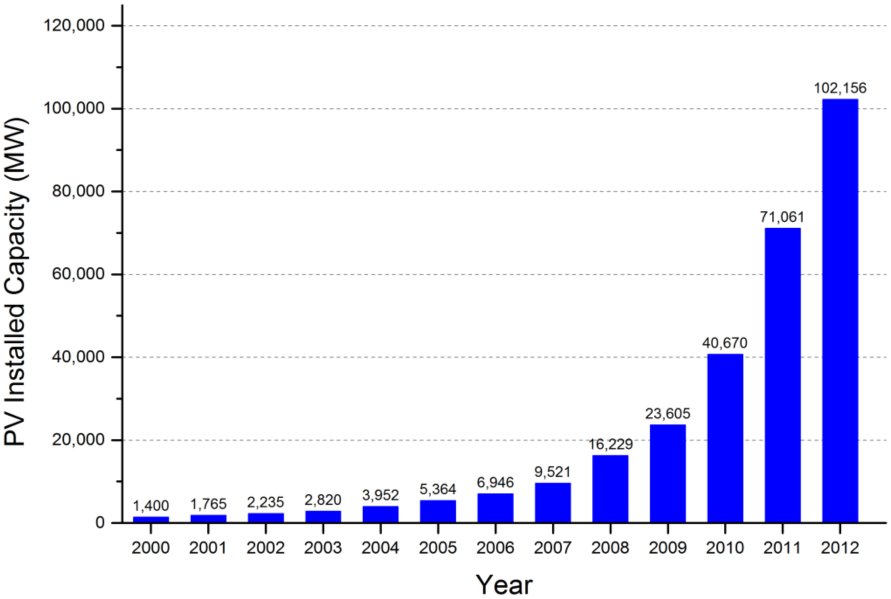

Figure 1.1 Global PV cumulative installed capacity 2000-2012. Data from EPIA [2]

Solar photovoltaic (PV), after hydro and wind power, now is the third most important renewable energy source in terms of globally installed capacity. It has experienced a remarkable growth at an average rate of 40%/year over the past decade (see Fig. 1.1) [2]. Through 2012, more than 100 GW of PV are installed globally and can produce at least 110 TWh of electricity every year, which currently provide 0.6% of the global electricity demand and 1.2% of the peak power demand [2]. In Germany, this figure is more than 5.6% of the total electricity production and has reached 50% of the peak electricity demand on some days [3]. At present, the typical electricity price generated from PV plants ($\sim\$0.27/\mathrm{kWh}$) has been less competitive than the prices from other traditional generation sources ($\sim\$0.10/\mathrm{kWh}$) [4]. However, the latter value will continue to rise due to an increased demand or at potentially higher carbon taxation rates and the most competitive recent PV installation is producing electricity below $\$0.06/\mathrm{kW}$. The electricity cost from PV plants is decreasing due to improved efficiency and manufacturing process and larger scale utilities. The crossover between these two prices, commonly called "grid parity", will take place in the relatively near future [5] (see Fig. 1.2). In fact, grid parity has been achieved in some regions such Southern California where solar insolation and the marginal cost of electricity are high [5].

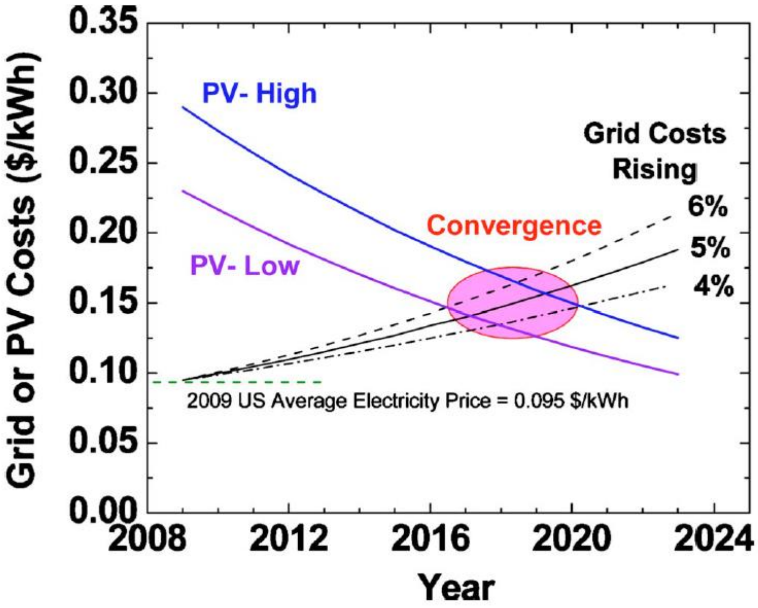

Figure 1.2 The electricity price trends generated from PV system and traditional sources from Wolden et al [5].

From the International Energy Agency's prediction [6], towards 2030, the electricity cost generated from typical large-scale utility PV system would decrease to $\$0.07-0.13/\mathrm{kWh}$, where the grid parity could reach in many regions. By 2050, PV global cumulative installed capacity could reach 3000 GW, providing 4500 TWh per year, which is equivalent to 11% of global electricity consumption. In addition, the installed PV utilities would reduce 2.3 gigatonnes of CO_2 per year and help to secure the energy supply and socio-economic development.

1.2 Thin-film Technologies in PV Industry

A thin-film solar cell (TFSC) is a cell made by depositing active layers a few microns thick on a substrate. Cadmium telluride (CdTe), copper indium gallium selenide (CIGS) and amorphous silicon (a-Si) are the three main thin-film technologies used in solar power production. Even though the crystalline silicon technology currently dominates the global PV industry with around 80% market share [2], there is a significant potential for large scale use of thin film solar cells in the long term due to the following reasons: a low material consumption compared to the fabrication of >100 μm thick silicon cells, low energy input for production and thus shorter energy “payback” time (~ 2 years for silicon, but < 1 year for thin films), the possibilities of flexible substrates which are suitable for building integrated PV (BIPV), and a large potential to close theoretical efficiency limit which help continuously lower the cost.

CIGS solar cells have achieved the conversion efficiency above 20% in cell scale [7] and 17.8% in module scale [8]. Due to its high efficiency and reduced manufacturing cost, CIGS technology is getting more popular than other thin-film technology. Now several companies, such as Solar Frontier [9], TSMC-Solar [10], and MiaSolé [11], have begun operating facilities with over $100\mathrm{MW/yr}$ production capacity.

1.3 Why Sputtered-Zn(O,S) buffer layer in CIGS TFSCs ?

In conventional a CIGS cell structure (see Section 2.1), CdS containing the hazardous material-Cd is widely used as the cell's buffer layer. In order to increase its environmental compatibility, a Cd-free buffer layer may be desirable in CIGS solar cells. In addition, the common CdS layer with a band-gap energy of about 2.4-2.5 eV, where most of the blue photons are absorbed, limits the photo current collection and thus cell efficiency. Therefore, an alternative buffer layer with higher band gap is needed to replace the CdS buffer layer. Zn(O,S), a Cd-free and abundant material with higher band gap (varying with oxygen content from 2.8 to 3.6 eV, see Section 2.1), is an attractive candidate. Fig. 1.3 shows the corresponding enhancement of photocurrent and conversion efficiency of Zn(O,S)/CIGS cells. The two cells in Fig. 1.3 were fabricated by using the same CIGS absorber but different buffer layer (CBD-CdS and sputtered-Zn(O,S), respectively) at NREL. Moreover, the band gap of the sputtered-Zn(O,S) can be modified by varying the oxygen fraction in the argon beam (see Fig. 2.2). Zn(O,S), thus, is likely to achieve better conduction-band offset when Ga expands the band gap of CIGS absorber, so as to obtain a higher efficiency CIGS cells [12, 13]. Finally, compared to chemical bath deposition and atomic layer deposition, the sputtering deposition of Zn(O,S) buffer layer is the most attractive process in terms of its suitability for inline, high throughput, and low-cost processing of junction [14].

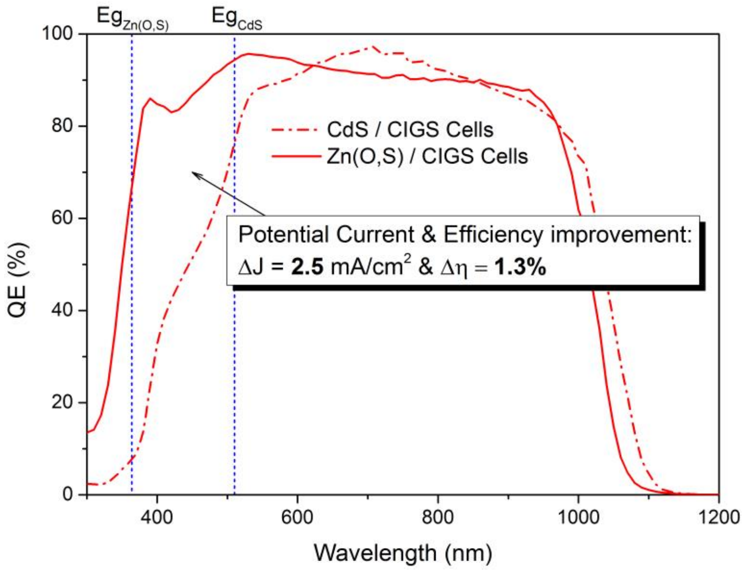

Figure 1.3 Quantum efficiency comparison between CdS/CIGS and Zn(O,S)/CIGS solar cells

Usually, a well-behaved J-V curve in solar cells is expected to achieve greater fill factor and thus a better cell performance. However, distorted J-V curves have been observed in some of the Zn(O,S)/CIGS cells fabricated at NREL and measured at CSU. Previous work from Pudov et al [15] suggested that a secondary barrier at the buffer-absorber interface is responsible for the J-V distortion in CdS/CIGS cells. Kanevce et al [16] found that, in the numerical simulation, the parameters that influence the barrier height, and hence the distortion, are the magnitude of the conduction-band offset (CBO), the doping of the p- and n- layers, the defect density of the CdS, and the thicknesses of the CdS layers. In this thesis, the J-V distortion in Zn(O,S)/CIGS cells will be investigated numerically and experimentally by following the secondary barrier theory.

Chapter 2 will review the device structure of CIGS cells, and the characterization and simulation techniques applied to illustrate J-V distortion. Chapter 3 will summarize the current transport mechanisms for the heterojunction CIGS cells and give an overview of explanation on J-V distortion. Chapter 4 will discuss two kinds of J-V distortions in Zn(O,S)/CIGS cells, J-V crossover and red kink, both of which have been investigated in different conditions. Chapter 5 will conclude the important information we have learned from this work.

Chapter 2

Background

2.1 Basics of CIGS Solar Cells

A typical CIGS solar cell, shown in Fig. 2.1, has a substrate configuration with a metal foil or soda-lime glass at the bottom and light entering the absorber through the top deposited layer. It consists of the following layers from bottom to top: a soda-lime glass at the bottom, a metallic Mo back contact layer, a p-type CIGS absorber, an n-type buffer layer, an undoped ZnO (i-ZnO) layer, and a conductive ZnO window layer, usually Al-doped ZnO.

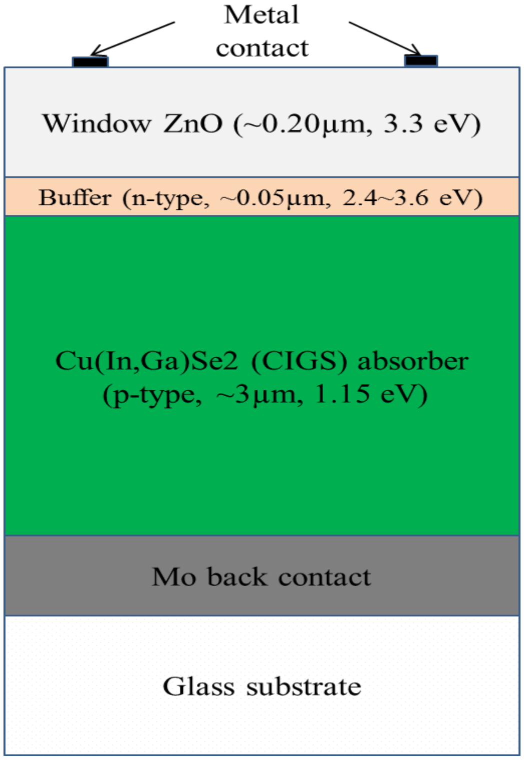

Figure 2.1 Device structure of a typical CIGS solar cell

The CIGS absorber with typical thickness of 2-3 µm is often deposited by using a co-evaporation process, and its band gap can be adjusted over a wide range by changing the ratio of

Ga to In in CIGS material deposition. The optimal empirical CIGS band gap is ~1.14 eV [17]. The n-type buffer has quite a few candidates, such as CdS, Zn(O,S), and In_2S_3, deposited with a variety of deposition techniques like chemical bath deposition (CBD), atomic layer deposition (ALD), and sputtering [18]. The band gap of the buffer layer depends on which candidate is chosen. The buffer layer we will discuss in this thesis is only sputtered Zn(O,S) material with the thickness of 50 nm. The band gap of Zn(O,S) can be modified by varying the oxygen fraction in the argon sputtering beam, seen in Fig. 2.2.

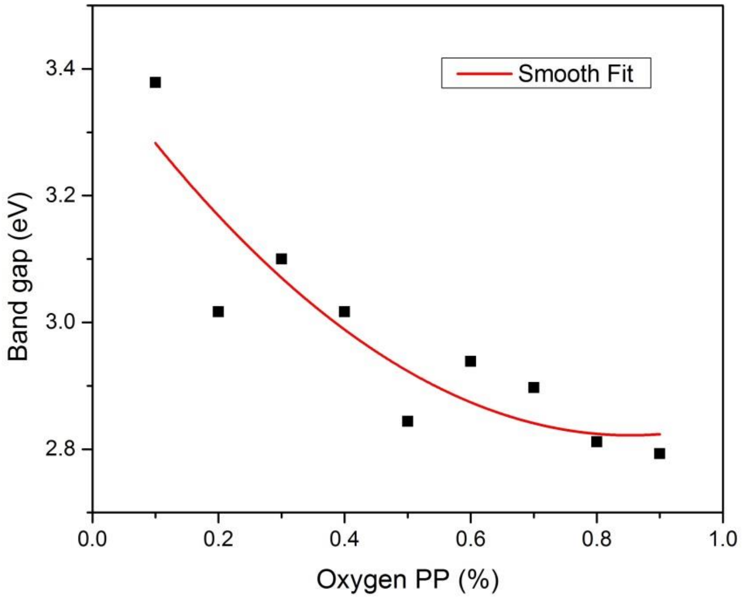

Figure 2.2 The relation between Zn(O,S) band gap and oxygen fraction in the argon sputtering beam for Zn(O,S) deposition

Now let us rotate the device structure in Fig. 2.1 left 90 degree (see Fig. 2.3). The red rectangle surrounded part of the top graph in Fig. 2.3 is the core of the cell, which is treated as a p-n junction photodiode. The bottom graph in Fig. 2.3 shows the energy band diagram of this photodiode. Most of the sunlight passes through the window ZnO and buffer layers due to their high band gap. When the photons reach the CIGS absorber, they will generate the electron-hole pairs. The photo-generated electron-hole pairs will be collected by the drift process to form the photocurrent. When the solar cell connects to the load, it will provide power output then.

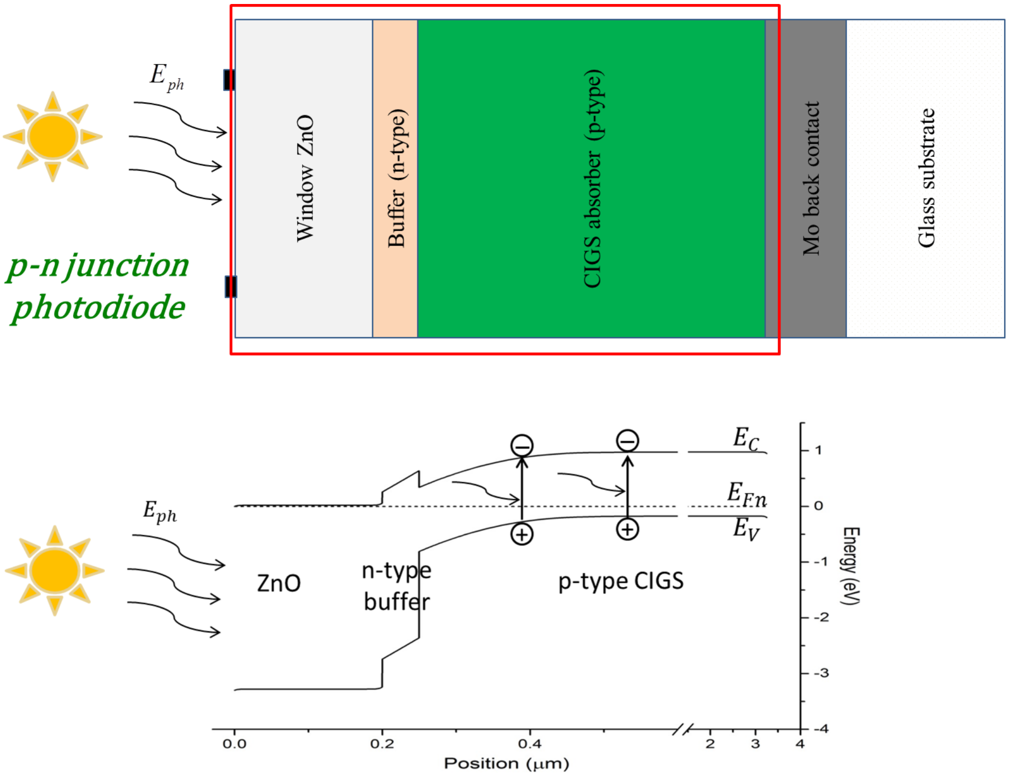

Figure 2.3 The device structure after left rotating 90 degree and the energy band diagram of its core p-n photodiode.

2.2 Current – Voltage Characterization

Light and dark current – voltage (J-V) measurements are fundamental to the identification of features, that may distort the J-V curves, especially for the work presented here, those from CIGS solar cells with sputtered Zn(O,S). Fig. 2.3 shows the simplified J-V measurement circuit. A Keithley programmable voltage source was used to apply voltage to a solar cell, typically from -0.5 V to 1.0 V. The actual voltage across the cell and the current flowing through the cell were measured with a Hewlett Packard multimeter, model 34401A. A LabVIEW program was used to control the measurement. The standard J-V measurement was done at the room temperature (+25 ℃) with two illumination conditions, dark and 100 mA/cm^2 white-light illumination. The standard illumination was achieved with a solar simulator, Solar Light Co., model XPS 400.

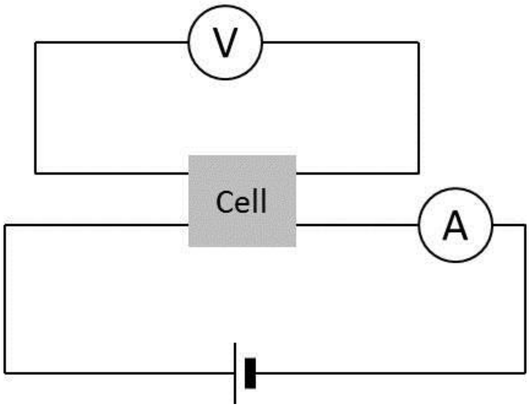

Figure 2.4 J-V measurement circuit

Fig. 2.5 shows the measured dark and light J-V curves for a well-behaved CIGS cell. Under illumination, the J-V curve shifts towards to the fourth quadrant. The following parameters are used to characterize a cell’s performance. At 0 V, there exists short circuit current J_{SC}; at open circuit condition, the open circuit voltage V_{OC} is measured; the deep grey area is the maximum power output P_{MP}; the ratio of P_{MP} to the product of J_{SC} and V_{OC} is the fill factor FF; the cell’s efficiency η is the ratio of P_{MP} and the incident light power P_{in}.

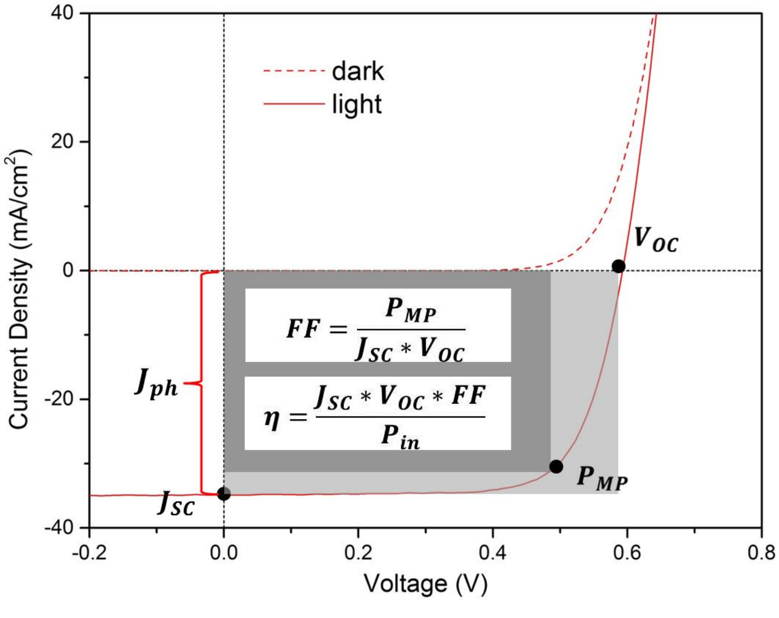

Figure 2.5 Measured dark and light J-V curves of a CIGS cell and the corresponding parameters

In addition, to investigate the effect of the secondary barrier on J-V distortion at the buffer-absorber interface in more details, J-V measurement at different illumination conditions and various temperature ranges were also performed. J-V measurements under red/blue-light illumination were achieved by using a 610-nm red/blue light filter, which only allows the light with wavelength greater/smaller than 610 nm transmitting, see Fig. 2.6. J-V measurements under different light intensities were done by using neutral density filters, with 1%, 10%, and 40% transmission. J-V measurements at a series of temperatures typically range from -35 ℃ to $+25$ ℃ were done by flowing cold nitrogen gas through a polymer box that encompassed the device and the mounting stage. J-V distortion, especially the red kink, may be affected by the photoconductivity of the Zn(O,S) buffer layer. To estimate the rate at which the high-energy blue photons affect the J-V distortion, we measured the J-V curves after cell exposure to high-energy photons for various lengths of time. Post-exposure J-V curves as a function of time without blue photons were also measured.

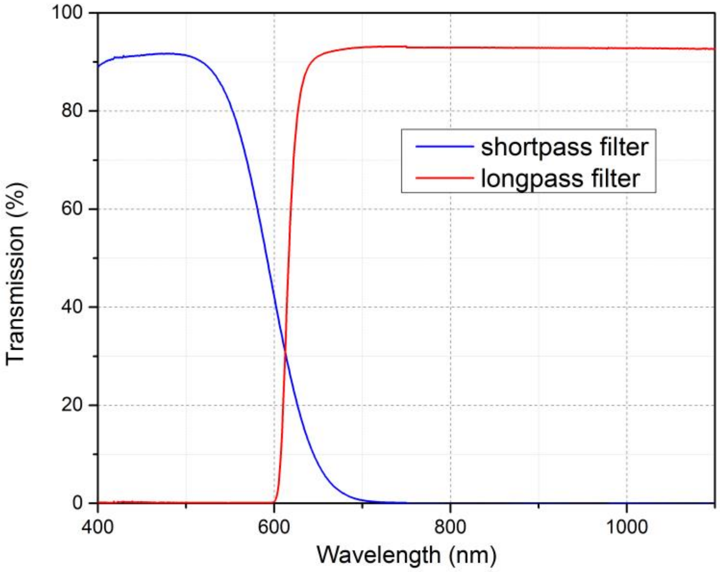

Figure 2.6 Transmission for both the red and blue light optical filters.

2.3 Device Modeling Software – wxAMPS

“wxAMPS” software [19] was designed at UIUC by Yiming Liu et al, following the physical principles of “AMPS-1D” software [20] developed at Pennsylvania State University by

S. Fonash et al. It allows the user to develop a band diagram and simulate the J-V and QE curves for a given set of parameters. The user interface of wxAMPS, seen in Fig. 2.7, uses a cross-platform library and provides quick data entry and improved visualization [21].

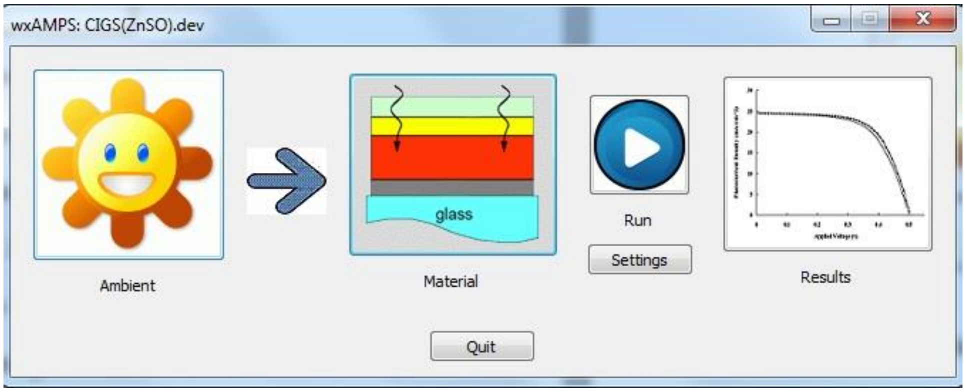

Figure 2.7 Primary user interface of wxAMPS

To simulate the J-V distortion of CIGS cells with sputtered Zn(O,S) and correlate it with experimental results, it is important to define a credible set of basic parameters for Zn(O,S)/CIGS cells. The baseline parameters chosen, based on Ref. [22], are shown in Table 2.1. The primary variations among baseline simulation cases presented here are the variations of the Zn(O,S) layer (grey area in Table 2.1). For variations in the Zn(O,S) oxygen fraction, the J-V characteristics were achieved through adjustment of the electron affinity of Zn(O,S); for variations in Zn(O,S) doping density, a probable range was chosen; for temperature- and light-intensity-dependent crossover cases, the experimental parameters were used; for similarly the red kink simulation cases, the red-light J-V curves were done by limiting the solar spectrum to the wavelengths greater than 610 nm.

Table 2-1 Basic parameters in Zn(O,S) / CIGS solar cells simulation

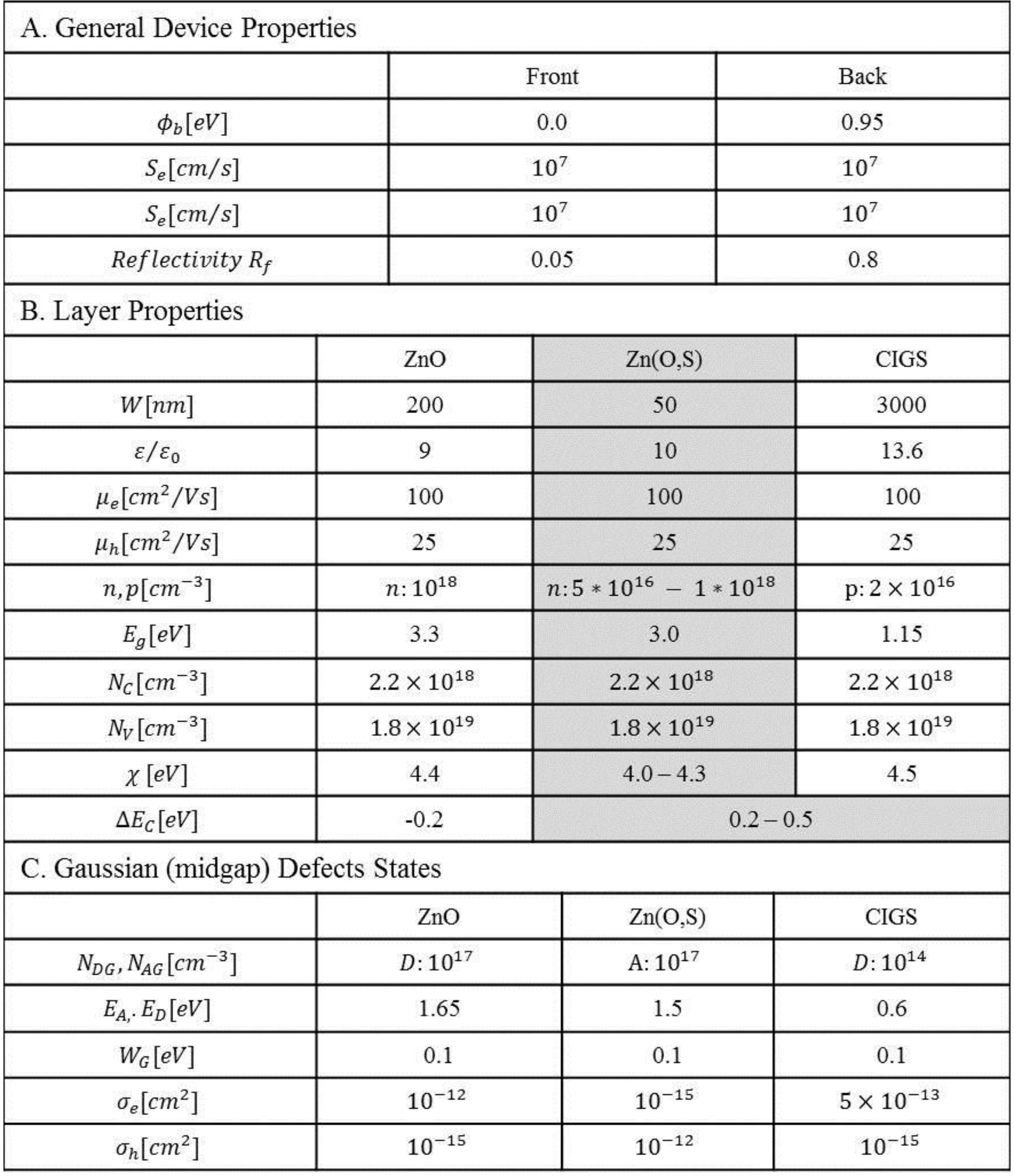

A. General Device Properties

	Front	Back
$\phi_b[eV]$	0.0	0.95
$S_e[cm/s]$	10^7	10^7
$S_e[cm/s]$	10^7	10^7
$Reflectivity\ R_f$	0.05	0.8

B. Layer Properties

	ZnO	Zn(O,S)	CIGS
$W[nm]$	200	50	3000
$\varepsilon/\varepsilon_0$	9	10	13.6
$\mu_e[cm^2/Vs]$	100	100	100
$\mu_h[cm^2/Vs]$	25	25	25
$n,p[cm^{-3}]$	$n: 10^{18}$	$n: 5 * 10^{16} - 1 * 10^{18}$	$\mathrm{p}: 2 \times 10^{16}$
$E_g[eV]$	3.3	3.0	1.15
$N_C[cm^{-3}]$	2.2×10^{18}	2.2×10^{18}	2.2×10^{18}
$N_V[cm^{-3}]$	1.8×10^{19}	1.8×10^{19}	1.8×10^{19}
$\chi\ [eV]$	4.4	4.0 – 4.3	4.5
$\Delta E_C[eV]$	-0.2	0.2 – 0.5	

C. Gaussian (midgap) Defects States

	ZnO	Zn(O,S)	CIGS
$N_{DG}, N_{AG}[cm^{-3}]$	$D: 10^{17}$	$\mathrm{A}: 10^{17}$	$D: 10^{14}$
$E_{A,}. E_D[eV]$	1.65	1.5	0.6
$W_G[eV]$	0.1	0.1	0.1
$\sigma_e[cm^2]$	10^{-12}	10^{-15}	5×10^{-13}
$\sigma_h[cm^2]$	10^{-15}	10^{-12}	10^{-15}

Chapter 3

Physical Explanation of J-V distortion

3.1 Current Transport Mechanisms

Before going through the discussion of J-V distortion, it is helpful to have an overview of the current transport mechanisms for p-n heterojunction CIGS cells. A common solar cell is essentially a large area p-n junction photodiode, where such of a diode is formed by asymmetric n-type and p-type semiconductors. For a typical CIGS cell, the n-type buffer layer and p-type CIGS absorber layer form a p-n heterojunction where the light is incident from the n-type side, and most of the light will be absorbed in the p-type CIGS and generate electron-hole pairs. The photo-generated carriers (electrons or holes) will be collected in three regions to form the photocurrent J_{ph}: the n-type neutral region, the space charge region (SCR) of the junction, and the p-type neutral region. In the two neutral regions (n- and p-type), the carriers are collected by a diffusion process; in the SCR, the carriers are collected by a drift process. In addition, under forward bias, electrons are injected into the p-type CIGS absorber and holes into the n-type Zn(O,S) buffer. These injected minority carriers (both electrons and holes) will be collected by the diffusion process to form the forward current J_F. Together, they are governed by "drift-diffusion" process, which happens in the bulk region. However, the current transport across the heterointerface barrier ϕ by thermionic emission and through the barrier ϕ by quantum tunneling are not considered. To comprehensively understand the current transport in the solar cell, all of the three types of current transport mechanisms above will be discussed (see in Fig. 3.1): (a) drift-diffusion transport for the bulk region [23] in Section 3.1.1, (b) thermionic emission across the interface [24, 25] in Section 3.1.2, and (c) quantum mechanical tunneling through the barrier at the interface [26] in Section 3.1.3.

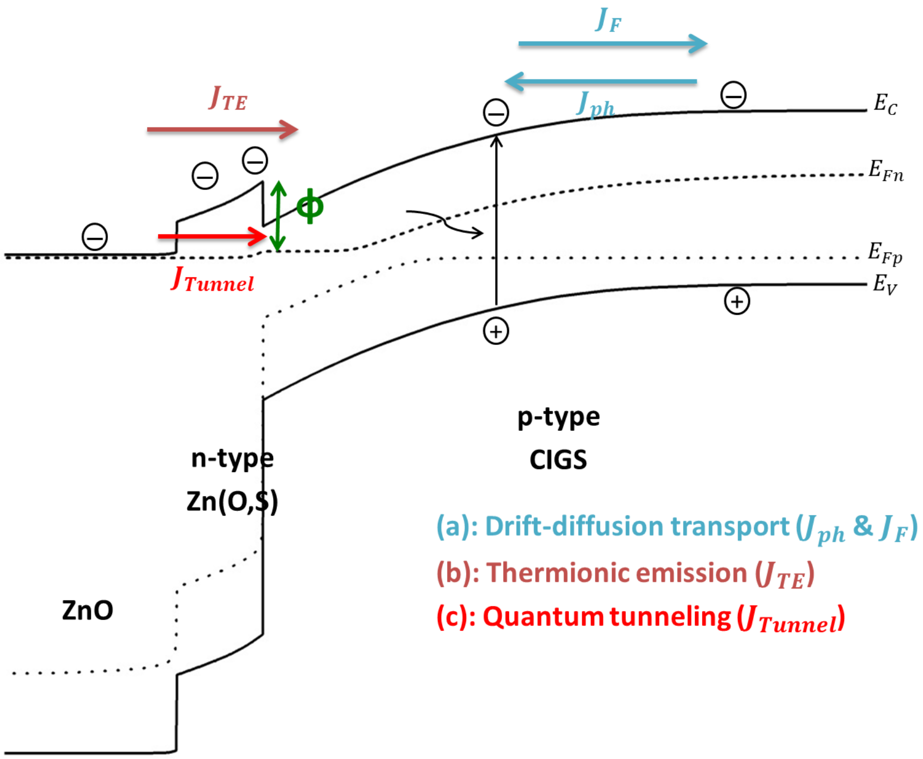

Figure 3.1 Electron current transport in the Zn(O,S)/CIGS cells, including three types of transport mechnisms, (a) drift-diffustion transport, (b) thermionic emission, and (c) Quantum tunneling

3.1.1 Drift-diffusion Transport in the Bulk Region

The basic equations governing the drift and diffusion of electrons and holes, Poisson's equation and the electron-hole current continuity equations, are expressed as follows [23]:

$$\frac{d\psi^2}{dx} = -\frac{q}{\epsilon}(p - n + N_D^+ - N_A^-) \qquad (3.1)$$

$$\frac{dJ_n}{dx} = q(R - G) \qquad (3.2)$$

$$\frac{dJ_p}{dx} = -q(R - G) \qquad (3.3)$$

Where ψ is the electrostatic potential, q the electron charge, ϵ the dielectric permittivity, p and n the hole and electron densities, N_D^+ and N_A^- the density of the ionized donor and acceptor, J_n and J_p the electron and hole current density, *R* the recombination rate, and *G* the generation rate. The term *R* is assumed to be specified by the Shockley-Read-Hall model:

$$R = \frac{pn - n_i^2}{\tau_{n0}(p+n_i)+\tau_{p0}(n+n_i)} \tag{3.4}$$

Where n_i is the intrinsic carrier density and τ_{n0} and τ_{p0} are the lifetimes for electrons and holes, respectively. In the bulk region, excluding the interface of the heterojunction cells, the electron and hole current equations can be expressed as [23]:

$$J_n = \mu_n n \nabla E_{Fn} \tag{3.5}$$

$$J_p = \mu_p p \nabla E_{Fp} \tag{3.6}$$

where μ_n and μ_p are the electron and hole mobility, and E_{Fn} and E_{Fp} are the quasi-Fermi level for electrons and holes, respectively.

Such drift-diffusion current transport model can be well used in the homojunction cells. However, it seems not that accurate when applied in the heterojunction cells because this model requires a continuous quasi-Fermi energy level across the interface, where there exists a spike in either conduction or valence band for heterojunction, leading to a discontinuity in quasi-Fermi energy [25]. Thus, other current transport mechanisms need to be considered at the interface.

3.1.2 Thermionic Emission Across the Interface

Another current conduction mechanism is thermionic emission. It is a majority carrier current, always associated with a potential barrier at the interface. Note that the critical parameter is the barrier height at the interface, not the shape of the barrier [23]. Fig. 3.2 (a) and (b) show the band diagram for a Zn(O,S)/CIGS cell in the dark at zero and 0.5-V forward bias, respectively. Note that the forward bias can lower the barrier ϕ at the interface; and the quasi-Fermi level for electrons decreases with the distance from the junction. The hole current has little influence on the current transport due to the large valence spike at the interface, and therefore only the conduction band and quasi-Fermi level for electrons will be analyzed.

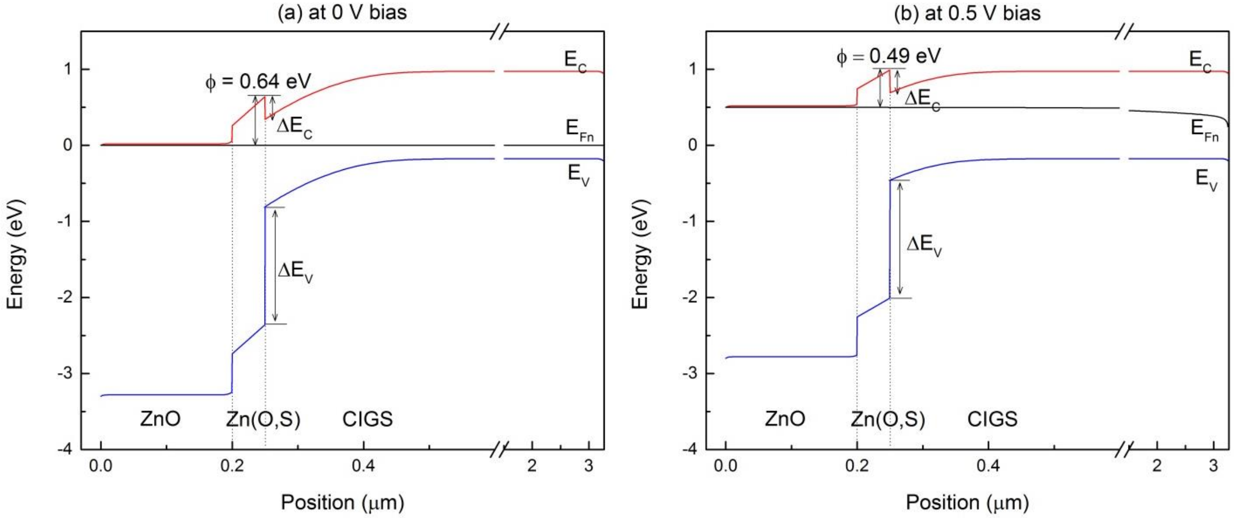

Figure 3.2 Band diagram for a Zn(O,S)/CIGS cell in the dark at (a) 0 V and (b) 0.5 V bias

Assume that thermionic-emission transport across the interface [23], the electron current across the conduction band spike is:

$$J_n = \int_{E_{fn}+\phi}^{\infty} q v_x dn \approx J_{TE} * e^{qV/kT} \tag{3.7}$$

and

$$J_{TE} = A^{*} T^{2} e^{-\phi/kT} \tag{3.8}$$

where $E_{fn} + \phi$ is the minimum energy required for thermionic emission, v_x, the carrier velocity in the direction of transport, J_{TE}, the thermionic emission current, $\phi = E_c - E_{fn}$, the barrier height, v_{th} the thermal velocity of electrons $\sim 10^7 cm/s$, A^* Richardson constant, and V the applied voltage. Note that the carrier densities far from the band edge are insignificant and close to E_c, and the velocities are similar to the thermal velocity, so the integral of Eq. 3.7 can also be approximated as [16]:

$$J_n \cong qnv_{th} \tag{3.9}$$

where v_{th} is the thermal velocity of electrons $\sim 10^7 cm/s$, and the free carrier density n in buffer layer is given by:

$$n = N_C \exp\left(-\frac{\phi}{kT}\right),\ \phi = E_C - E_{fn} \tag{3.10}$$

From Eq. 3.9 and 3.10, we can conclude that the maximum electron current through the junction is determined by the free carrier density in buffer layer and therefore the barrier height at the interface. In addition, the conduction-band offset (CBO) at the interface caused by the adjustment of the electron affinity χ of the buffer can shift this barrier up and down assuming χ_{CIGS} is fixed, which will be discussed in Section 3.2.

3.1.3 Quantum Tunneling Through the Interface

Tunneling is a quantum-mechanical phenomenon. In classical mechanics, the carriers cannot pass through the barrier which has a higher energy than the carrier; however, in quantum mechanics, such case can happen. Especially, at low temperature and/or high doping density, the carrier transport by tunneling process becomes significant [26]. When tunneling process dominates the behavior at an interface [21, 26], the current through that interface, $\mathrm{J_I}$, is composed of thermionic emission current $\mathrm{J_{TE}}$ and an intra-band tunneling current, expressed as:

$$\mathrm{J_I} = (1 + \delta)\mathrm{J_{TE}} \tag{3.11}$$

where δ is the tunneling coefficient composed by a complex integral. For simplicity, the effect of the tunneling current transport on the J-V distortion will not be considered in the thesis.

3.2 Secondary Barrier Theory

3.2.1 Current transport inside the CIGS solar cell

The current transport mechanisms have been detailed discussed in Section 3.1. Since quantum tunneling will not be covered in this thesis, we now simplify the current transport inside the solar cell shown in Fig. 3.3. From this figure, we see that, in the p-type CIGS side, there are two current components, the photocurrent J_{ph} which is collected by the diffusion process and the forward current J_F which is collected by the drift process. Their sum is the net current J, which approximates to the thermionic current J_{TE} flowing across the secondary barrier at the interface. The thermionic emission current J_{TE} is dominated by the secondary barrier and has a major effect on the J-V distortion.

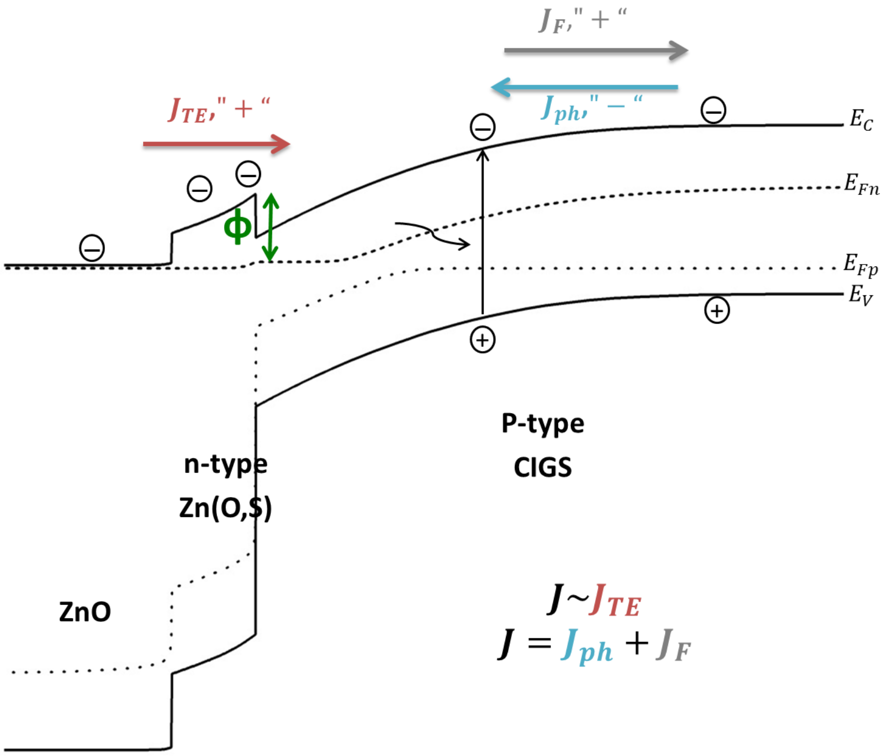

Figure 3.3 Electron current transport inside a CIGS solar cell

3.2.2 How Thermionic Current Depends on the Secondary Barrier

From Eq. 3.8 in Section 3.1.2, we have known that the thermionic current is determined by both the temperature and the secondary barrier, see in Fig. 3.4. After rearranging Eq. 3.7 at V = 0, the barrier height is expressed by:

$$\phi = E_c - E_{fn} = kT \cdot \ln(\frac{A^* T^2}{|J|}) \tag{3.12}$$

At room temperature (298 K) and a typical value of J_{SC} (i.e. $J \sim J_{SC} = 35\ \mathrm{mA/cm^2}$), the maximum distortion-free barrier height would be $\phi_{max} = 0.46\ eV$ is required. If the barrier height exceeds this value, the current collection across the interface will be limited and additional drift fields are needed to insure the electron pass across the interface, and there will be distortion of J-V (details in Section 3.2). We call this mechanism as "the secondary barrier rule".

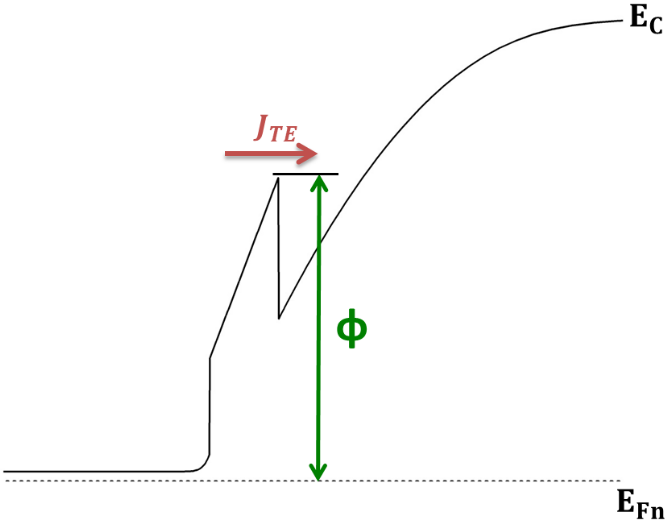

Figure 3.4 The energy band diagram around the buffer-absorber interface

3.2.3 Factors to Determine the Secondary Barrier ϕ

In Section 3.2.2, we have pointed out that the thermionic current is governed by the secondary barrier rule. The key question is what factors have an effect on the barrier ϕ. In this thesis, we summarize four factors: the conduction-band offset - ΔE_C, the Zn(O,S) electron doping density - $n_{Zn(O,S)}$, the photoconductivity of Zn(O,S), and the operating temperature.

Conduction-band Offset - ΔE_C

The conduction-band offset (CBO) is the conduction-band discontinuity between the n-type Zn(O,S) and p-type CIGS. The individual band gaps of Zn(O,S) and CIGS are controlled by the O/S and Ga/In ratios, respectively, and the resulting offsets can range from +1.3 eV in the "spike" direction to -0.7 eV in the "cliff" direction if the full range of the two ratios is considered [13]. The cells discussed in the thesis are of fixed Ga/In ratio in the CIGS absorber ($E_{g(CIGS)} \sim 1.1\ eV$) but variable O/S ratio in the Zn(O,S) buffer ($E_{g(Zn(O,S))} \sim 2.8 - 3.4\ eV$, see in Fig. 2.2), which means there is a stable band structure for CIGS but not for Zn(O,S). In addition, Persson et al [27] suggested that the O/S ratio in Zn(O,S) can affect both the conduction band and valence band, see in Fig. 3.5. Therefore, we may conclude that the cells' CBOs in the thesis only come from the Zn(O,S) side.

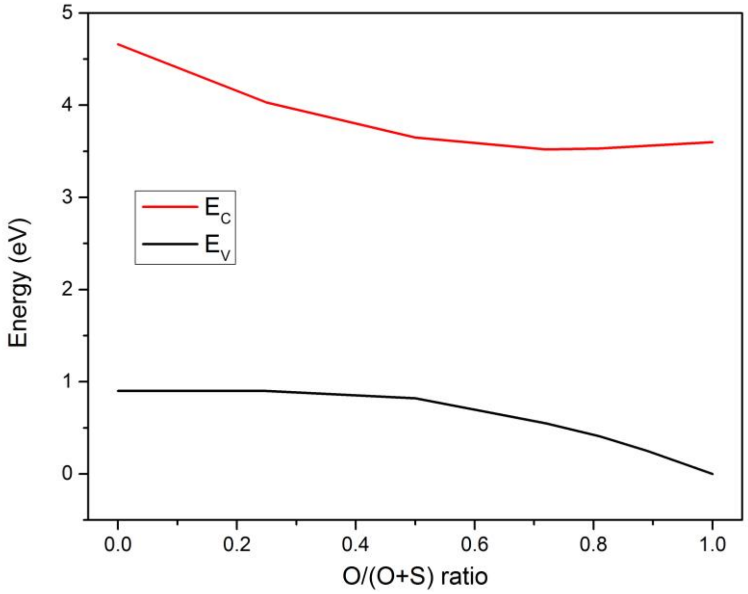

Figure 3.5 Energy band diagram for Zn(O,S) as a function of O/(O+S)[27]

The CBO can be achieved through adjusting the electron affinity of Zn(O,S) in the numerical simulation. Fig. 3.6 shows the secondary barrier height for three different CBO. It is dearly seen that, the secondary barrier height increases with the conduction-band offset.

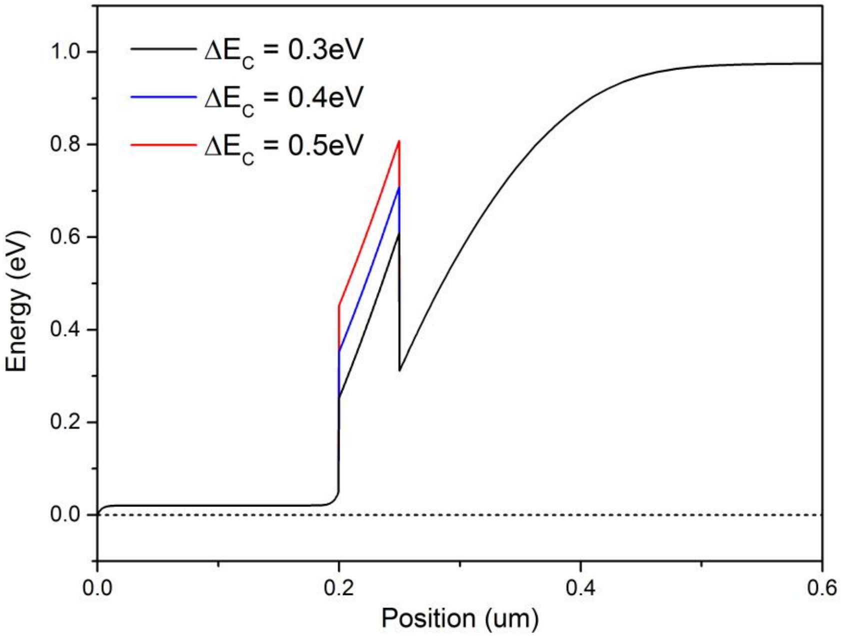

Figure 3.6 The Secondary barrier height for different ΔE_C

Zn(O,S) electron doping density - $n_{Zn(O,S)}$

The second factor is the Zn(O,S) electron doping density $n_{Zn(O,S)}$. It is observed that, from Eq. 3.10,

$$n = N_C \exp\left(-\frac{\phi}{kT}\right),\ \phi = E_C - E_{fn} \qquad (3.10)$$

the larger the electron density in Zn(O,S), the smaller the barrier height at the interface. Fig. 3.6 shows the barrier difference for two electron doping levels in Zn(O,S) buffer. In the low level doping, the barrier height is increased significantly with respect to the high doping case.

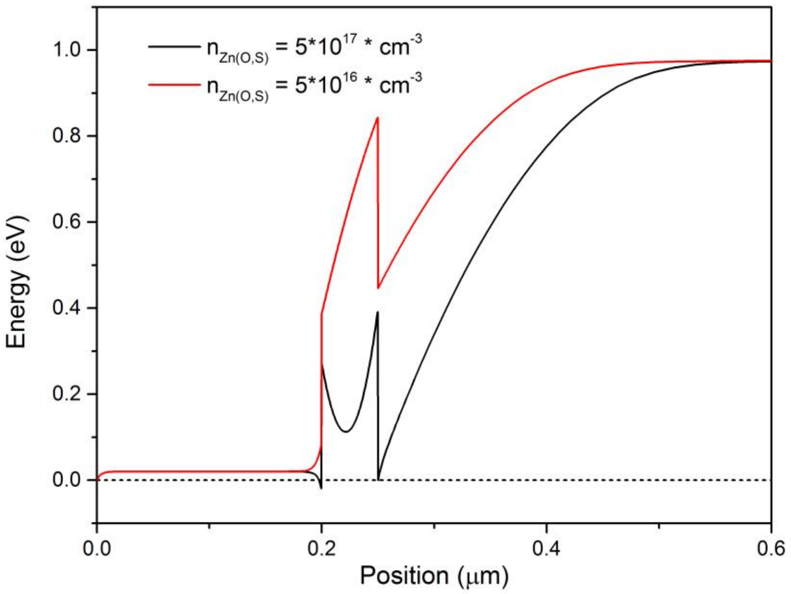

Figure 3.7 The secondary barrier height for two different electron doping levels

Photoconductivity of Zn(O,S)

The photoconductivity of both CdS and ZnS has been observed in [28, 29], and causes the cell performance change under different illumination conditions [30, 31]. Now we assume that the "photo-doping" process exists in n-type Zn(O,S) layer as well. Fig. 3.8 shows the change of Zn(O,S) effective doping density from the dark to white-light illumination condition. Suppose that the electron doping density of Zn(O,S) is $\mathrm{n_{Zn(O,S)}} = 5 \times 10^{16} * cm^{-3}$, and a high density of acceptor-like deep level defect $N_{AG} = 2 \times 10^{16} * cm^{-3}$ located near the midgap of the buffer layer. In Fig. 3.8(a), in the dark, most of electrons ionized from the donor state are captured by the defect states. So the free electron density $\mathrm{n_{Zn(O,S)}}$ is decreased to $N_D - N_{AG} \sim 3 \times 10^{16} * cm^{-3}$ and now the Zn(O,S) buffer layer is compensated. In Fig. 3.8(b), under illumination, the photons with energy bigger than the band gap of Zn(O,S) (i.e. $\mathrm{E_{g(Zn(O,S))}} \sim 2.8\, eV$) will generate the electron-hole pairs. Ideally, there are nearly $2 \times 10^{16}\ \text{photons} * s^{-1} * cm^{-2}$ which can generate an equivalent amount of the electron-hole pairs (calculated from the standard AM 1.5

Solar Spectrum, [32]). The photo-generated holes are coulomb attracted to the acceptor-like defects. The photo-generated electrons $2 \times 10^{16} * s^{-1} * cm^{-2}$ are not affected and thus increases the free electron density of Zn(O,S) to the original level, $n_{Zn(O,S)} \sim N_D$.

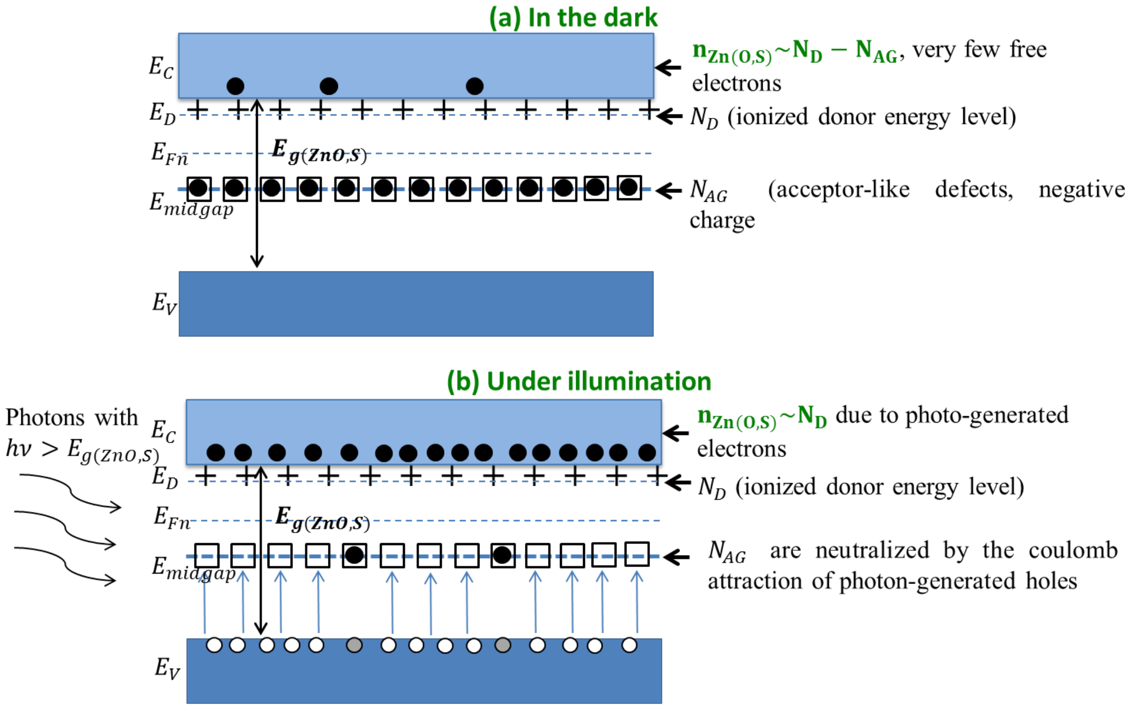

Figure 3.8 The doping level in Zn(O,S) (a) under dark conditions, and (b) under illumination.

From the previous part in this section, we have concluded that the increased free carrier density can lower the secondary barrier at the absorber/buffer interface. Clearly if a n-type Zn(O,S) layer with such a “photo-doping” property as a partner in a p-n junction, it will have a major effect on the cell’s energy band under illumination. Fig. 3.8 shows the barrier difference for dark and illumination cases. Under illumination, the barrier height is reduced with the help of the high energy photons.

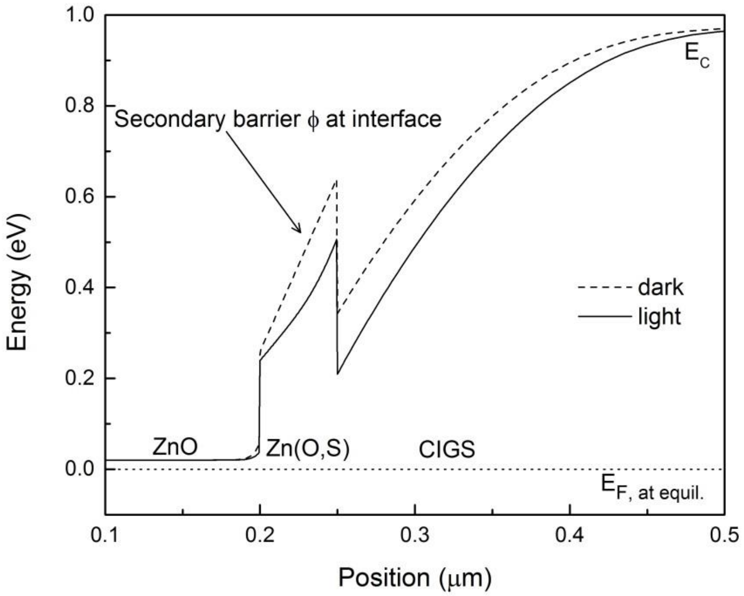

Figure 3.9 Secondary barrier lowering due to the photo-doping

The Operating Temperature

As discussed in Section 3.2.2, the barrier height is also related to the operating temperature. Fig. 3.10 shows an approximately linear correlation between the operating temperature and the maximum distortion-free barrier height ϕ_{max}. As the operating temperature decreases, the reduced ϕ_{max} will limit the electron current to flow across the interface more seriously and consume more voltage to achieve the same J as the high-temperature barrier. The small table in Fig 3.10 has list all the maximum distortion-free barriers ϕ_{max} for the corresponding operating temperature range from 238 K to 298 K.

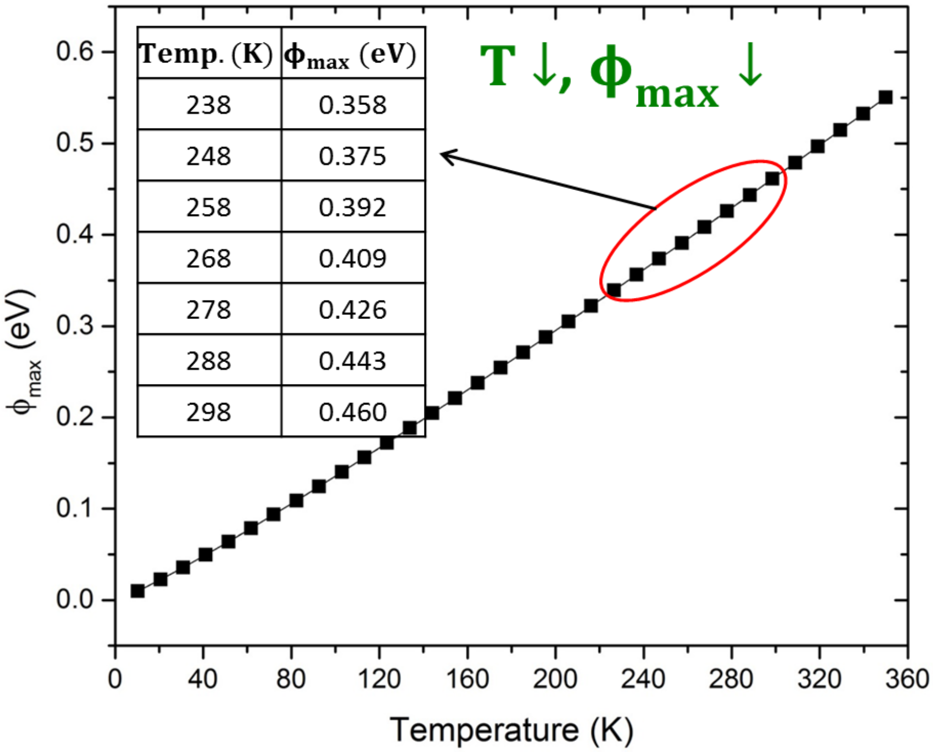

Temp. (K)	ϕ_{max} (eV)
238	0.358
248	0.375
258	0.392
268	0.409
278	0.426
288	0.443
298	0.460

Figure 3.10 Correlation between the temperature and the maximum distortion-free barrier

For instance, in Fig. 3.11, even though we have the same actual barrier height $\phi = 0.46\ eV$ at different temperature, one is at low T, another at high T, they have different max distortion-free barrier. So for low T, there is fewer amount of thermionic current which will leads to greater J-V crossover (discussed later).

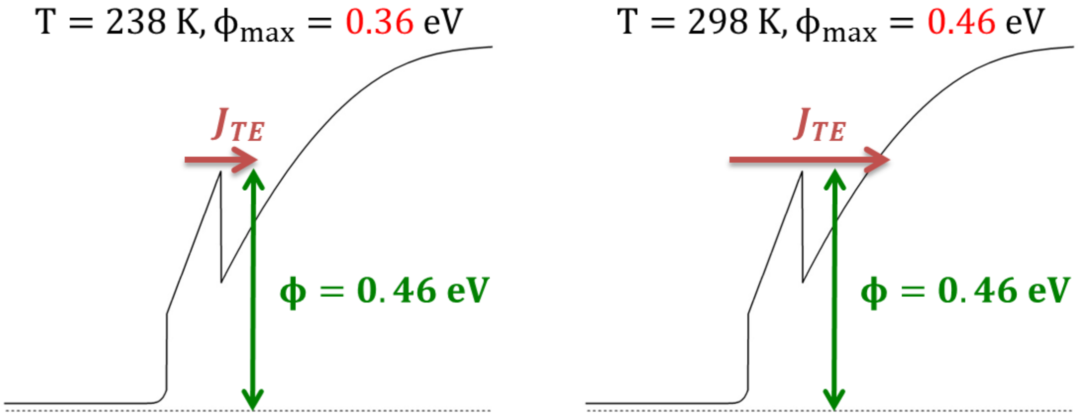

Figure 3.11 The thermionic current difference at two different temperatures.

3.3 J-V Distortion Explanation

Distortion to current – voltage curves have been commonly reported in CIS or CIGS solar cells with a variety of buffer layers, such as CBD CdS, ZnS(O,OH), and InS(O,OH) [15, 30, 31]. In our current research, we found that the CIGS cells with sputtered Zn(O,S) buffer layer also show the J-V distortion, as seen in Fig. 3.12.

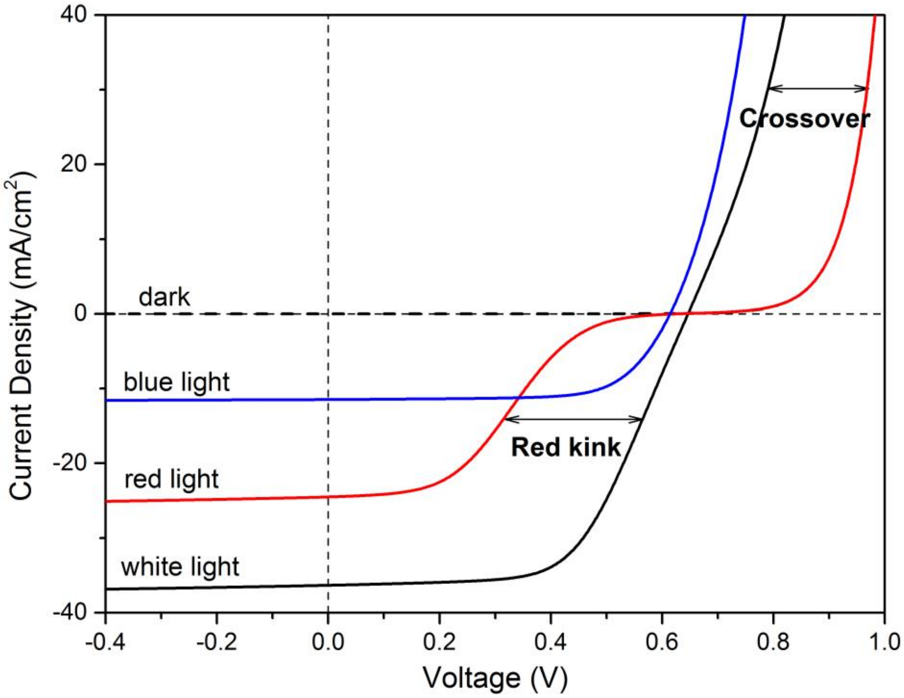

Figure 3.12 Typical J-V distortion in CIGS cells with sputter Zn(O,S)

In general, the J-V distortion in CIGS can be divided into J-V crossover and J-V red kink. The J-V crossover refers to a failure of dark/light superposition of their current-voltage curves; the J-V red kink refers to the distortion of J-V curves under only long-wavelength-photon illumination (>610 nm) at initial forward bias. Many researchers [15, 30, 31] have investigated the physical mechanism of these J-V distortions on the traditional CdS – CIGS solar cells, and their models suggests that such J-V distortions are due to the conduction band secondary barrier at the buffer-absorber interface. In this thesis, we are going to discuss the two kinds of J-V distortions of sputtered-Zn(O,S)/CIGS solar cell with the secondary barrier theory (Section 3.2).

3.3.1 Light-dark J-V Crossover

J-V crossover between dark and light J-V curves is commonly observed in the current-voltage measurement of CIGS cells. A typical J-V crossover is shown in Fig. 3.13. We can see that to achieve the same amount of current density at forward bias, the dark curve need to consume more voltage compared to the light curve. Now we apply the secondary barrier theory to the light-dark J-V crossover analysis.

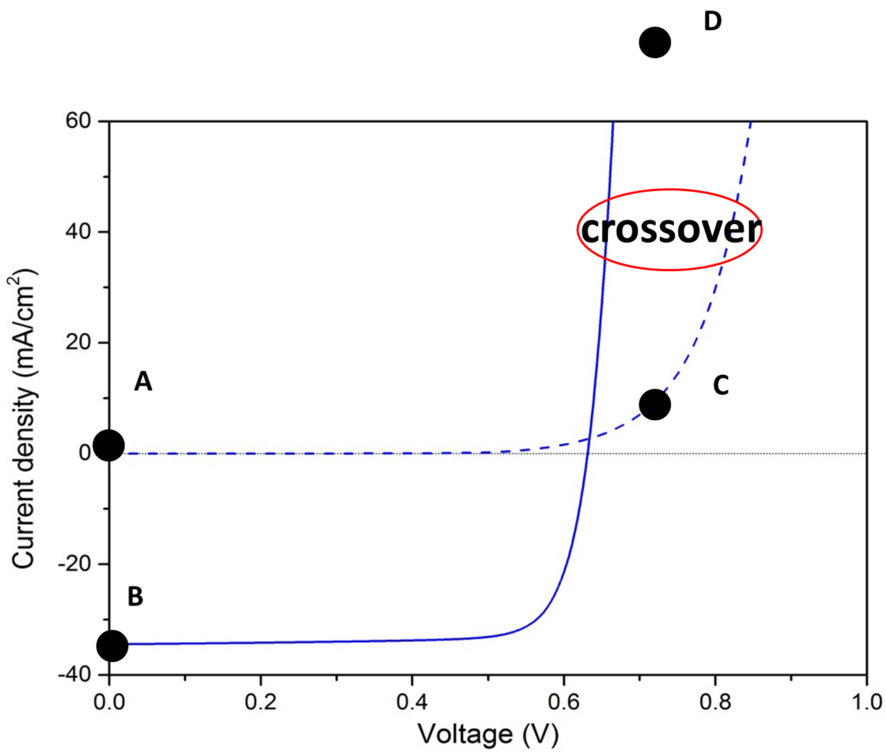

Figure 3.13 Typical J-V crossover between dark and light curves

Here, assume that the thermionic emission (J_{TE}), discussed in Section 3.1.2, is the primary current transport mechanism across the buffer/absorber interface of in solar cells. At room temperature (298 K), the maximum distortion-free barrier height ϕ_{max} is $0.46\ eV$. If the barrier height exceeds this value, additional drift fields are needed to insure the electron pass across the interface. In addition, there exists the forward current J_F under forward bias above Voc and photocurrent J_{ph} under white-light illumination, respectively. Fig. 3.14 shows the conduction band E_c and electron quasi-Fermi level E_{fn} in the dark and under illumination and at zero and 0.7 V forward bias.

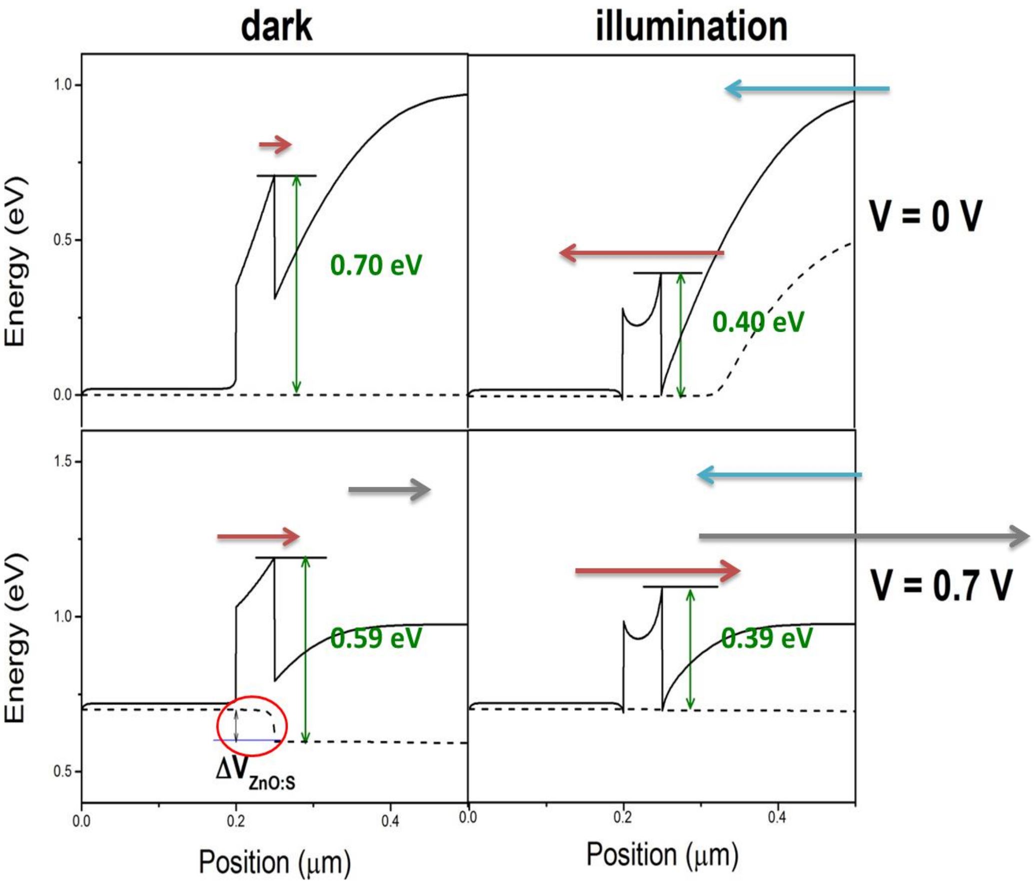

Figure 3.14 Conduction band and quasi-Fermi level (a) in the dark at 0 V, (b) under illumination at 0 V, (c) in the dark at 0.7 V, and (d) under illumination at 0.7 V.

(a) At 0 V, dark, no photocurrent J_{ph} and forward current J_F. Due to the high barrier 0.70 eV there is little thermionic current J_{TE}. Thus, net current J is zero, represented by point A in Fig. 3.14.

(b) At 0 V, illumination, there is photocurrent in the p-type CIGS side. And due to the "photoconductivity" the barrier height reduces to 0.40 eV, which allows the photo-generated electrons to flow across barrier. The net current is equal to the photocurrent, represented by point B.

(c) At 0.7 V, dark, although high barrier, but the applied voltage helps electrons pass through the spike at the cost of a small voltage drop across Zn(O,S) ($\Delta V_{Zn(O,S)}$), see point C.

(d) At 0.7 V, light, due to the "photoconductivity", the barrier is reduced to 0.39 eV, allowing the photocurrent passing across. Although the photocurrent J_{ph} can offset the net current J, the large forward current J_F still helps increase J in point D is greater than in point C.

Note that, it consumes more voltage for point C in the dark to achieve the same current as point D under illumination, which corresponds to the voltage drop across Zn(O,S) in the energy band diagram in part (c). Such superposition failure of dark and light curve leads to the crossover.

3.3.2 J-V Red Kink

A typical kinked J-V curve under red-light illumination in CIGS cells is shown in Fig. 3.15. At reverse or small forward voltage bias, the cell has well-behaved current collection proportional to the J-V curve under white-light illumination. At forward bias between 0.2 V to Voc, it shows an impeded current collection, called "red kink", and at forward bias above Voc until 0.8 V the red-light J-V curve overlaps with the dark one. Fig. 3.16 shows the conduction band E_c and electron quasi-Fermi level E_{fn} under white-light and red-light illumination at 0.3 V bias. Note that under red-light illumination, most free electrons in the Zn(O,S) buffer layer are trapped in the deep-level defects of Zn(O,S) due to the lack of high energy photons (see "the photoconductivity of Zn(O,S)" in Section 3.2).

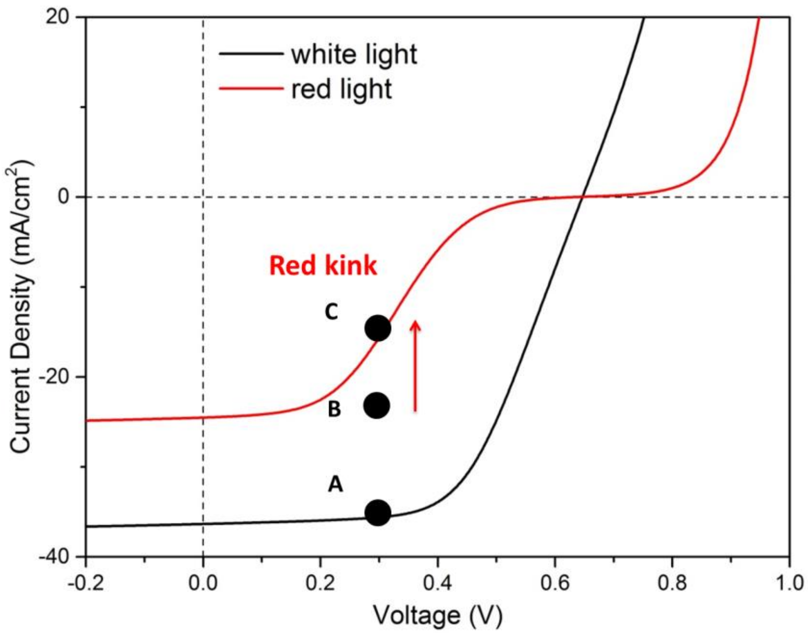

Figure 3.15 Typical J-V red kink under red-light illumination

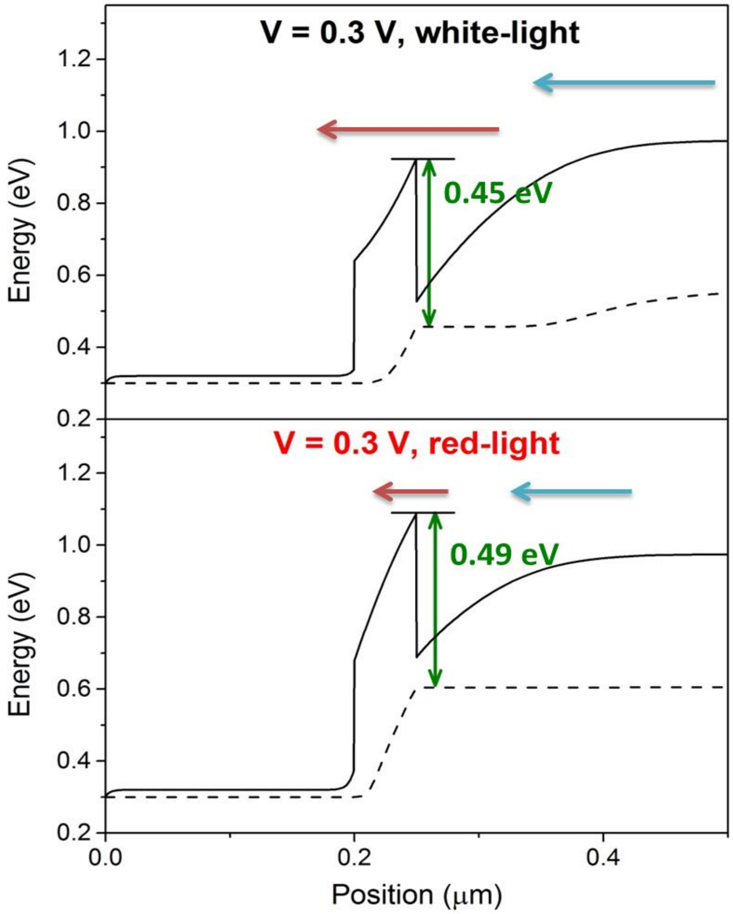

Figure 3.16 Conduction band and quasi-Fermi level (a) under white-light illumination at 0.3 V, and (b) under red-light illumination at 0.3 V.

(a) At 0.3 V, white-light illumination, the low barrier has no effect on thermionic current J_{TE}. Thus, it allows the photo-generated electrons to flow across barrier. Meanwhile, the 0.3 V bias is too small to allow the current through the p-n junction increasing rapidly. So there is little forward current J_F. The net current J is still the photocurrent, represented by point A in Fig. 3.15.

(b) At 0.3 V, red-light illumination, the barrier increases to 0.49 eV which is greater than $\phi_{max} = 0.46\ eV$, limits the photocurrent pass across the barrier. In addition, there is little J_F. Thus, the net current decreases from point B to C in Fig. 3.15. It leads to a kinked J-V curve.

Chapter 4

Investigation on Experimental J-V Distortion

In this chapter, we will investigate on the J-V distortion in different experimental cases and correlate each case with a specific physical explanation of J-V distortion. Section 4.1 and 4.2 cover a series of detailed discussions about both the J-V crossover and J-V red kink under red-light illumination, respectively. In addition, a quantitative J-V distortion comparison between simulated and experimental results is given in Section 4.3 to set up a straightforward understanding on how well the experimental J-V distortions correspond to the numerical simulation results.

4.1 J-V Distortion – Crossover

In Section 3.3, we have pointed out that the J-V crossover is due to the secondary barrier at the absorber-buffer interface. Theoretically, the barrier height can be modulated by the conduction-band offset (CBO) at the interface, the doping density of the buffer layer, and the experimental factors, such as illumination condition and temperature (Section 3.2). Experimentally, the J-V crossover we have observed is associated with the different recipes in cell fabrication, such as varying oxygen content and indium doping in the buffer. The measurement of CBO and doping density of the buffer is a challenging task and it is difficult to immediately tell the accuracy of their results. So the challenge remaining is how to explain and identify the experimental J-V crossover with the unknown change of the CBO and doping densities of Zn(O,S) layers in our cells. The numerical simulations in the following sections may allow us to have greater insight in the correlation between the experimental J-V crossover with those physical parameters.

4.1.1 Effect of Oxygen on Crossover

A key parameter for the sputter deposition of Zn(O,S) is the oxygen fraction in the argon beam. The trend of the O/(S+O) ratio in the sputtered Zn(O,S) films versus the oxygen fraction in the argon beam has been found by Grimm et al [33]: the greater the amount of oxygen fraction in the argon beam at a fixed temperature, the higher the oxygen composition in the Zn(O,S) films (Fig. 4.1). The oxygen fraction was varied with a range from 0.3% to 1.0% in our cell fabrication which corresponds to O/(S+O) in the films with a range measured by XPS from 10% to 60% (denoted by the red oval in Fig. 4.1).

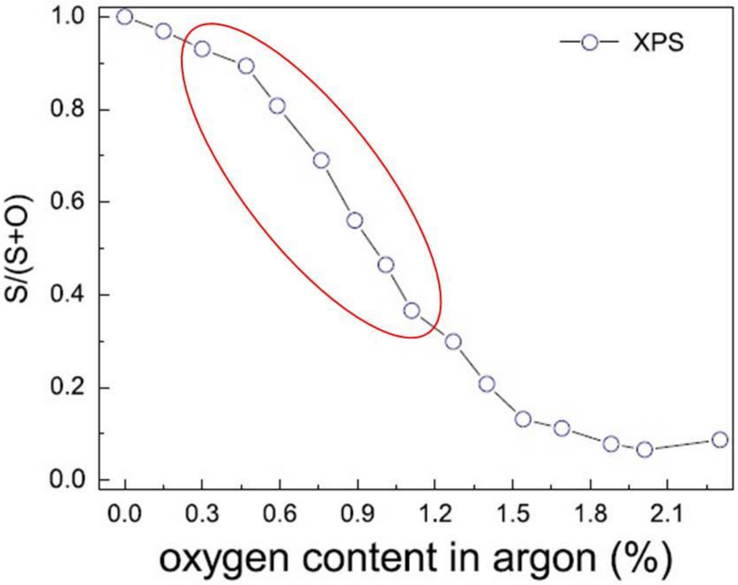

Figure 4.1 Composition of sputtered Zn(O,S) films as a function of the oxygen fraction in sputter argon gas. Data from Grimm et al [33].

The J-V crossover between dark and light curves, observed in most cases, is found to vary with the oxygen fraction in the sputter beam. Fig. 4.2 shows that, the lower the oxygen fraction in the Zn(O,S) sputtering process, the larger J-V crossover observed.

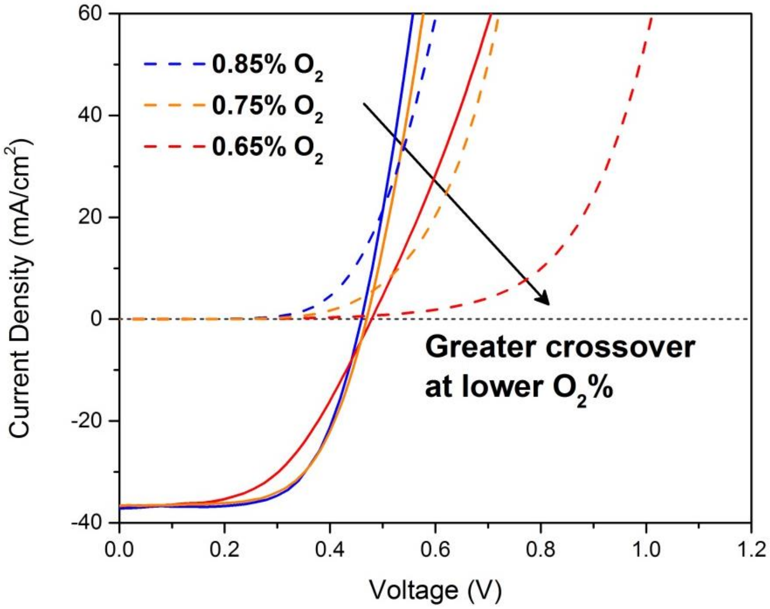

Figure 4.2 J-V crossover at various oxygen fraction in sputtering Zn(O,S)

The question is whether it is reasonable to relate such a J-V crossover caused by the variation of oxygen content to the secondary barrier at the interface. Persson et al [27] found that the conduction-band edge of alloy $ZnO_{1-x}S_x$ increases strongly for x > 0.5. In other words, the CBO between Zn(O,S) and CIGS decreases with an increased oxygen ratio in Zn(O,S) films if O/(S+O) is smaller than 50%. By following the finding by Grimm et al [33], we may conclude that the 0.3-1.0% oxygen fraction in the argon gas corresponds to 10-50% O/(O+S) in the films. It is hypothesized, therefore, that the CBO-induced barrier is responsible for the J-V crossover for the case with varying oxygen content in Zn(O,S). To verify this hypothesis, the numerical simulation is employed.

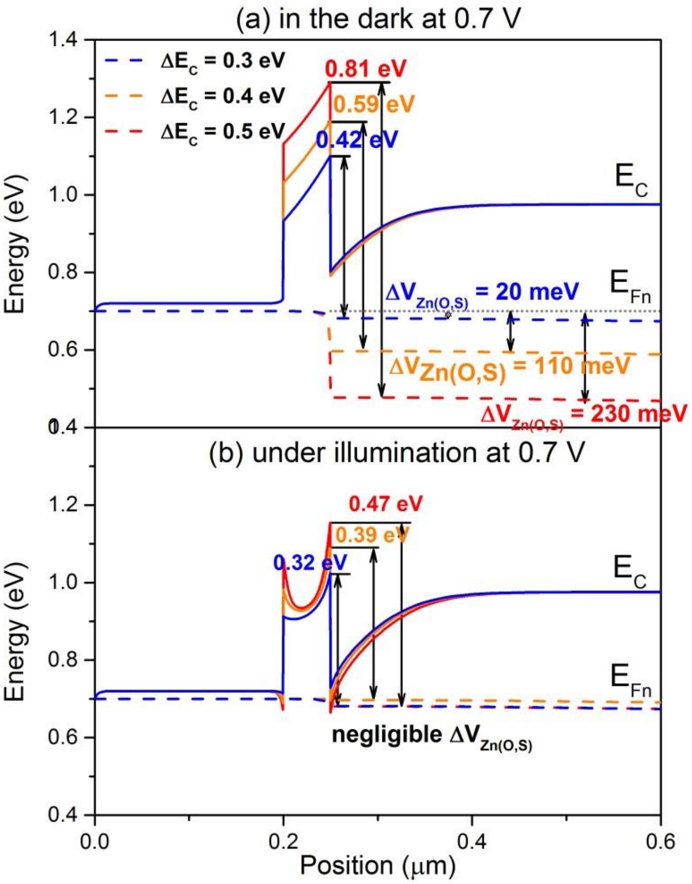

Figure 4.3 Simulated band diagrams for a variety of CBO - ΔE_C at 0.7 V bias: (a) in the dark, and (b) under illumination

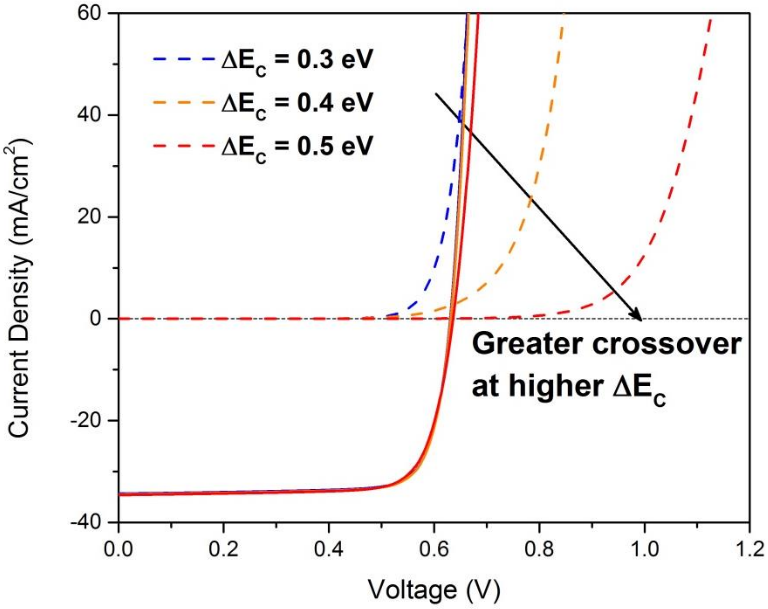

Figure 4.4 Simulated J-V crossover for various values of ΔE_C

In Fig. 4.3(a), at 0.7 V bias in the dark, the barrier height increases along as ΔE_C is increased, which has been discussed in Section 3.1.2. Note that for the cases $\Delta E_C = 0.4\ eV$ and $\Delta E_C = 0.5\ eV$, the barrier heights are bigger than the required 0.46 eV (calculated from Eq. 3.11) which limits the standard-spectrum electron current flowing through the interface from left to right. In addition, there is an obvious voltage drop $\Delta V_{Zn(O,S)}$ for the quasi-Fermi level in all ΔE_C cases, but the voltage drop increases with an increased CBO in the band structure. This can be explained as follow: due to the higher barrier height, the cells with higher ΔE_C have to sacrifice more voltage at the interface (greater $\Delta V_{Zn(O,S)}$) to allow the same amount current to flow through the interface as the lower ΔE_C in the dark. Under illumination, however, the barrier heights for all cases are significantly reduced, which can explained by the photoconductivity of the Zn(O,S) layer (Section 3.2). The low barrier heights, $\phi = 0.32\ eV$ and $\phi = 0.39\ eV$ for $\Delta E_C = 0.3\ eV$ and $\Delta E_C = 0.4\ eV$, respectively, no longer restrict the electron current flowing anymore and their J-V curves almost overlap with each other. Nevertheless, there is a small light J-V discrepancy between $\Delta E_C = 0.3\ eV$ (or $\Delta E_C = 0.4\ eV$) and $\Delta E_C = 0.5\ eV$ due to a slightly higher barrier ($\phi = 0.47\ eV$) in the $\Delta E_C = 0.5\ eV$ case. Despite of such a small discrepancy, there is little voltage drop for the quasi-Fermi levels among all the three different ΔE_C cases, which means their forward current rises at a lower forward bias than with the comparable dark J-V curves. In conclusion, there is more right shift from the dark J-V curves to the light one for higher ΔE_C cases due to a greater barrier height except for the $\Delta E_C = 0.3\ eV$ case.

Now let's turn to the comparison between Fig 4.2, the experimental J-V crossover with varying oxygen fraction in Zn(O,S) sputtering, and Fig. 4.4, the simulated J-V crossover at a variety of ΔE_C. In Fig. 4.2, the lower the oxygen fraction in sputtering Zn(O,S) process, the greater the J-V crossover; in Fig. 4.4, the higher the CBO (ΔE_C), the greater the J-V crossover. In the previous discussion, we just concluded that with an increasing amount of oxygen content in Zn(O,S) films, the CBO in the cells will decrease. Thus we can conclude that the greater J-V crossover with an increasing amount of oxygen content in the Zn(O,S) films is due to the increase of CBO- induced barrier height.

4.1.2 Effect of Zn(O,S) Doping on Crossover

CIGS cell fabrication at NREL has included Zn(O,S) buffer layers that were deposited by RF magnetron sputtering in Ar/O_2 ambient from two different targets: the non-indium(In)-doped ZnS target and the In-doped ZnS target. We found that the J-V crossover in In-doped Zn(O,S) cells is negligible, but is quite pronounced in non-In-doped Zn(O,S) cells (Fig. 4.5). The Zn(O,S) buffer layers in the two cells we will discuss in Fig. 4.5 are both sputtered at the same conditions (0.7% O_2 in the argon beam with substrate temperature 200 ℃), except for different ZnS targets (with and without In doping).

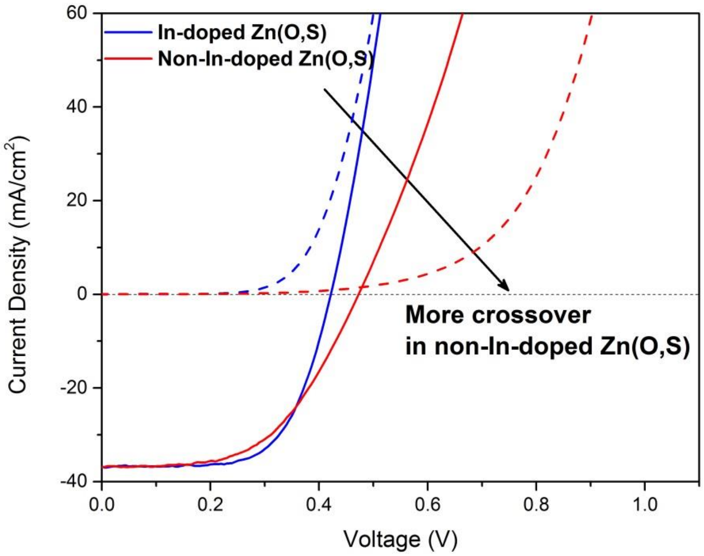

Figure 4.5 Experimental J-V curves for CIGS cells with In-doped and non-In-doped Zn(O,S)

Since indium doping helps increase the free electron density in n-type ZnO films [34], we propose that the free electron density of Zn(O,S) films can also benefit from doping indium in

Zn(O,S) buffer layers. Meanwhile, note that the barrier height at the buffer-absorber interface, which plays a key role in the J-V crossover formation, can be modulated by the free electron density in the buffer layer (Section 3.2). One may thus hypothesize that the J-V crossover difference between the In-doped and non-In-doped Zn(O,S) buffer is due to the variation of the free electron density ($n_{Zn(O,S)}$) caused by indium doping in Zn(O,S). Now we introduce the numerical simulations to verify the hypothesis. It is assumed that the only effect of the In-doping of the target is to modify the electron carrier density of Zn(O,S) in the resulting larger.

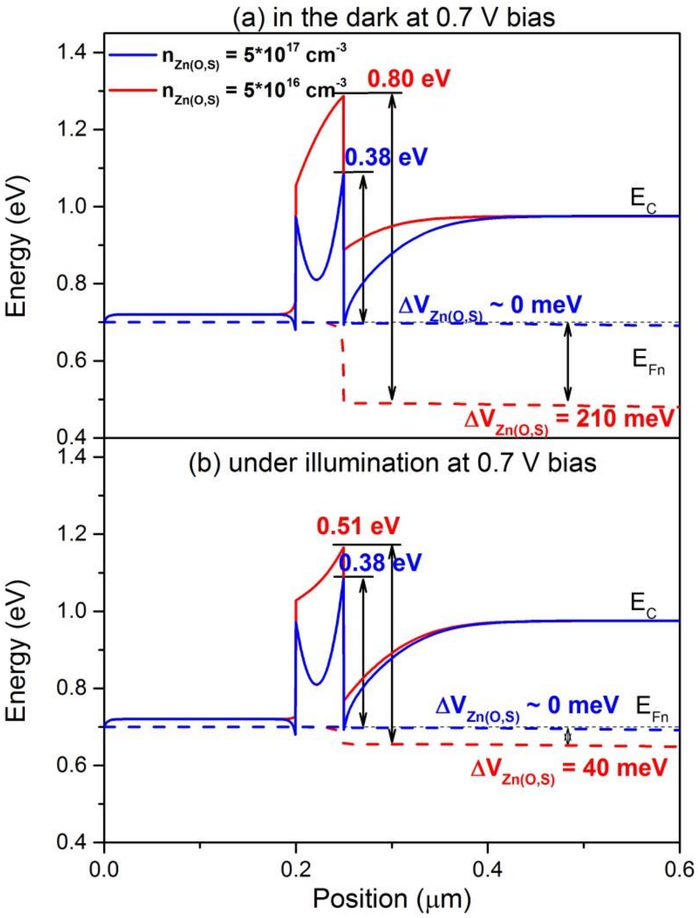

Figure 4.6 Simulated band diagrams for different $n_{Zn(O,S)}$: (a) in the dark at 0.7 V bias, and (b) under illumination at 0.7 V bias.

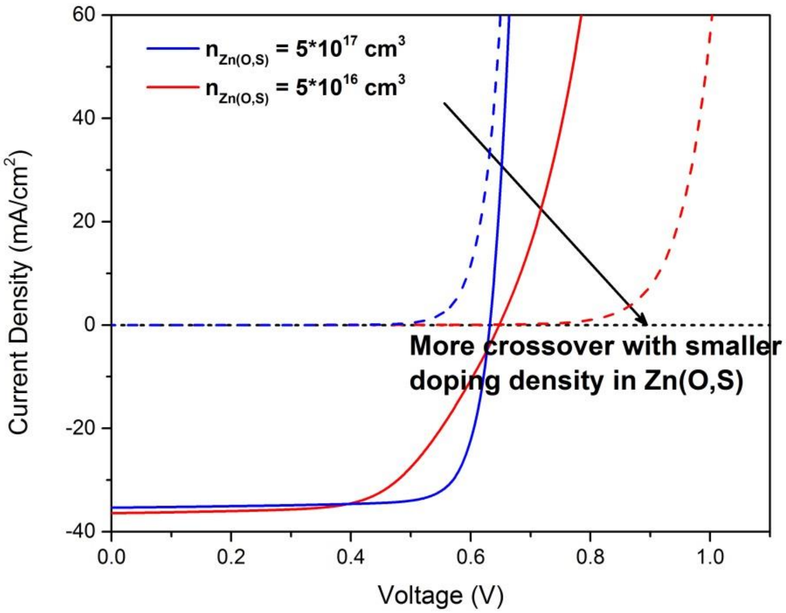

Figure 4.7 Simulated J-V crossover at different $n_{Zn(O,S)}$

Fig. 4.6 shows the conduction bands and quasi-Fermi levels for two different $n_{Zn(O,S)}$ in the dark and under illumination at 0.7 V bias. Fig. 4.7 shows the corresponding J-V curves for different $n_{Zn(O,S)}$. In Fig. 4.6(a), in the dark at 0.7 V bias, the secondary barrier ($\phi = 0.80\ eV$) for the cell with $n_{Zn(O,S)} = 5 * 10^{16} cm^{-3}$ is nearly twice higher than that for the cell with $n_{Zn(O,S)} = 5 * 10^{17} cm^{-3}$, which severely blocks the standard-spectrum electron current flowing through the interface from left to right (the highest barrier to allow current to flow is $\phi = 0.46\ eV$); the quasi-Fermi level for $n_{Zn(O,S)} = 5 * 10^{16} cm^{-3}$ is thus no longer continuous at the interface and drops to a lower energy level ($\Delta V_{Zn(O,S)} = 210\ meV$). In Fig. 4.6(b), under illumination at 0.7 V bias, the barrier height for $n_{Zn(O,S)} = 5 * 10^{16} cm^{-3}$ is reduced due to the photoconductivity of Zn(O,S) (Section 3.2) and there is a much smaller voltage drop ($\Delta V_{Zn(O,S)} = 40\ meV$) across the interface as well. The above results indicates that at the cost of voltage drop in the Zn(O,S), the dark J-V curve for $n_{Zn(O,S)} = 5 * 10^{16} cm^{-3}$ shifts to higher voltage. For the higher doping density case ($n_{Zn(O,S)} = 5 * 10^{17} cm^{-3}$), there is little change on the secondary barrier and the quasi-Fermi level both in the dark and under illumination: the barrier height is low enough ($\phi = 0.38\, eV$) to allow the electron current to flow through the interface and the voltage drop $\Delta V_{Zn(O,S)}$ approximates to zero, so there is no crossover between the dark and light J-V curves for higher doping density. From the simulation, therefore, we can conclude that with a decreased doping density in Zn(O,S) buffer, there is a greater crossover between its dark and light J-V curves. The simulation results now allows one to relate the free electron density ($n_{Zn(O,S)}$) and J-V crossover to Indium doping in Zn(O,S).

4.1.3 Light-intensity Dependence

In Section 4.1.1 and 4.1.2, we have discussed the effects of the Zn(O,S) buffer layers' internal properties (CBO and doping density) on the J-V crossover. Now we turn to investigate the external effect of light-intensity on the J-V crossover. A Zn(O,S) buffer layer of the CIGS cell was deposited with non-In-doped ZnS target at 0.65% O_2 fraction in the argon gas. Fig. 4.8 shows that the J-V crossover between dark and light curves varies with the light-intensity: the smaller the light-intensity, the closer the J-V curve is to the dark J-V for forward currents. To explore the inside physical mechanisms of such a J-V crossover trend, it is useful to simulate the cell's band diagrams and the corresponding J-V characteristics, and compare the simulated J-V curves with the experimental J-V ones.

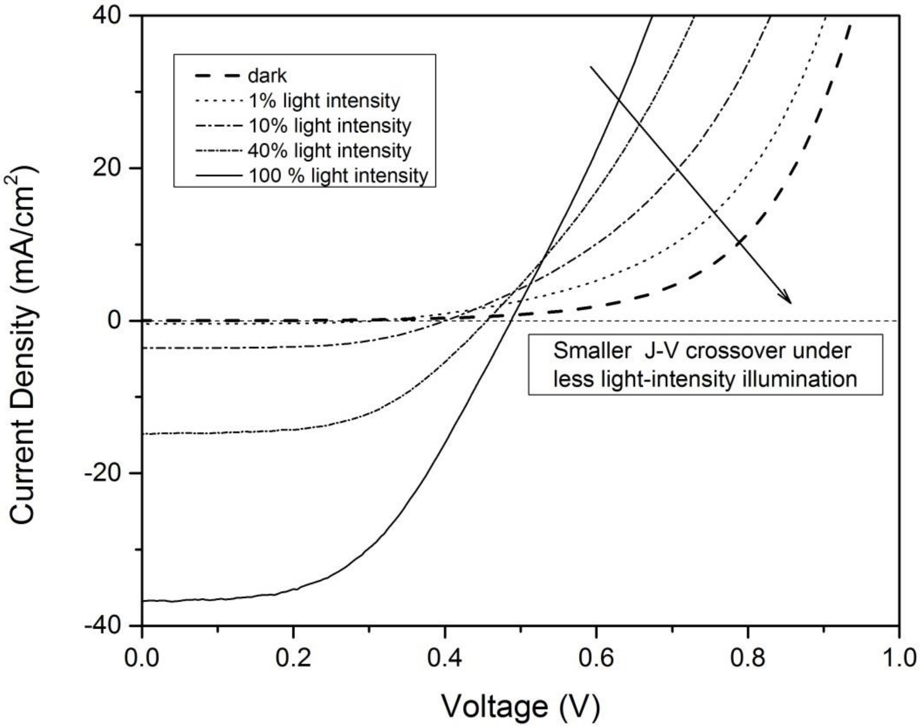

Figure 4.8 Experimental J-V curves under varying light-intensity illumination

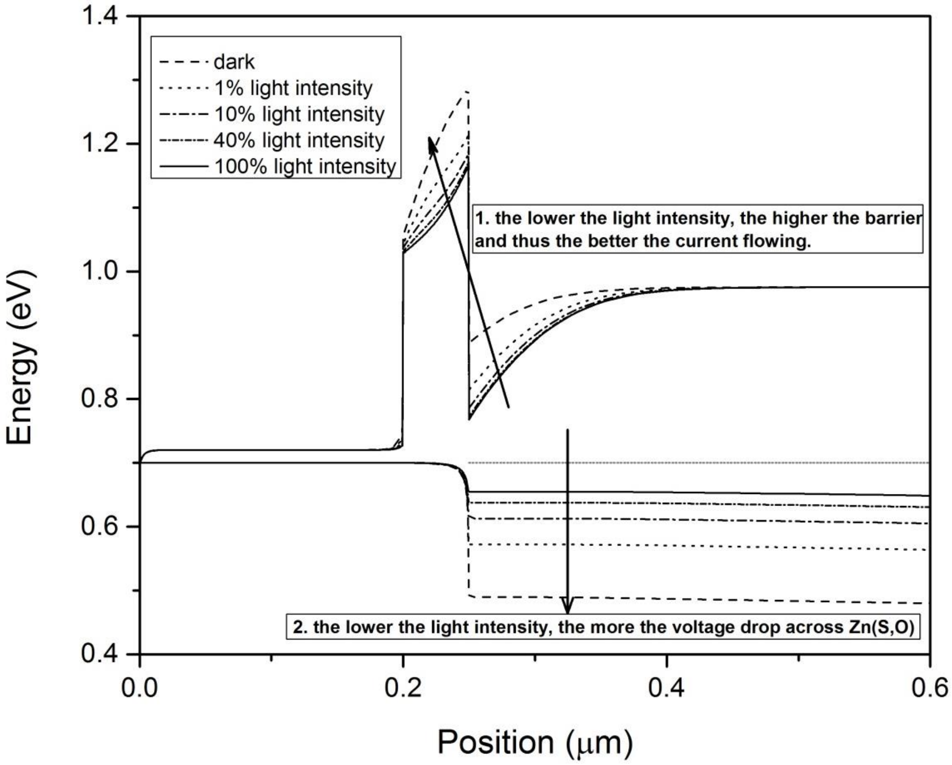

Figure 4.9 Simulated band diagrams at 0.7 V bias under varying light-intensity illumination

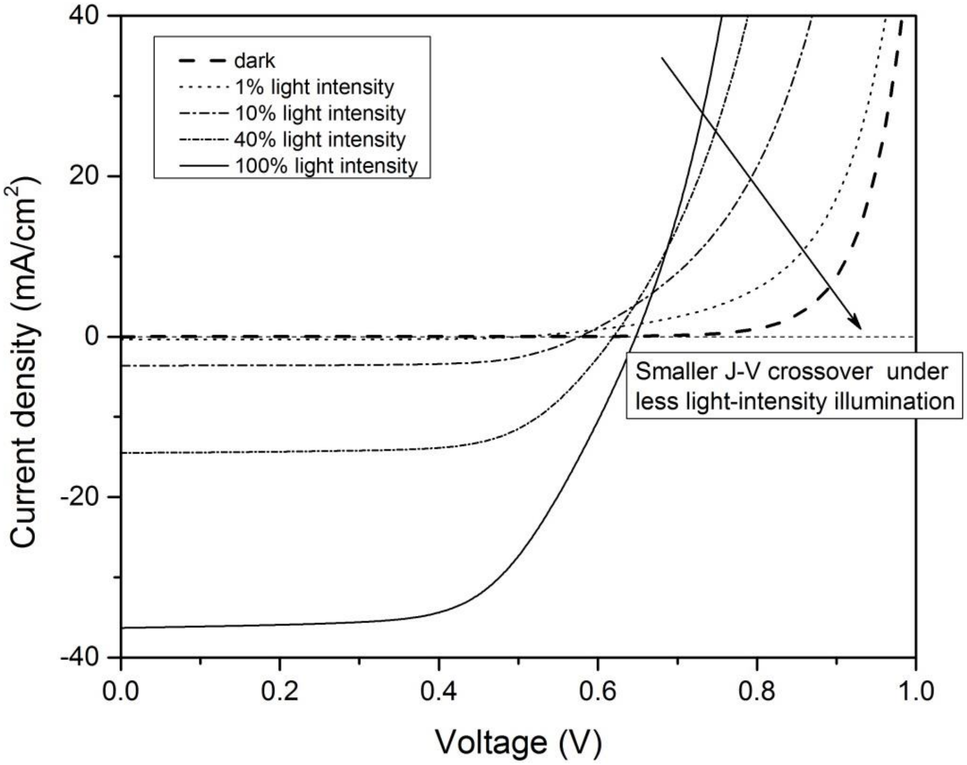

Figure 4.10 Simulated J-V curves under varying light-intensity illumination

Fig. 4.9 shows that, the height difference of the secondary barrier under varying light-intensity illumination and the corresponding variation in the quasi-Fermi level. In Fig. 4.10, the simulated J-V curves under varying light-intensity illumination show the same J-V crossover trend as the experimental case: the smaller the light-intensity, the smaller the J-V crossover between light and dark curves. Fig. 4.9 provides an explanation. In Fig. 4.9, the barrier height is higher when the light-intensity is reduced; the highest secondary barrier exists in the dark. The higher secondary barrier limits electron current flowing through the interface. As a result, the quasi-Fermi level will drop at the interface at a greater degree, which can explained by the photoconductivity of the Zn(O,S) buffer layer (Section 3.2). Under lower light-intensity illumination, there are a smaller amount of photons with $h\nu > E_{g(Zn(O,S))}$ which can excite the buffer layer to release the trapped electrons from the deep-level defect state, and thus the free electron density in Zn(O,S) decreases. From Section 4.1.2, we showed that with lower doping density in the Zn(O,S) buffer, requires a larger voltage drop $\Delta V_{Zn(O,S)}$ across the Zn(O,S) to achieve the same amount of current at high bias as for higher doping density. In other words, the lower light-intensity will push the corresponding J-V curve right towards the dark J-V curve at high bias ($V > V_{OC}$), and thus a smaller J-V crossover takes place.

4.1.4 Temperature Impact

In addition to the light intensity, operating temperature plays a key role in the cells' performance. Now we turn to investigate the effect of operating temperature on the J-V crossover. A Zn(O,S) buffer layer of the CIGS cell was deposited with non-In-doped ZnS target at 0.85% O_2 in the argon gas. The experimental J-V crossover is often temperature-dependent (see Fig. 4.11). In general, the lower the operation temperature is, the greater the J-V crossover.

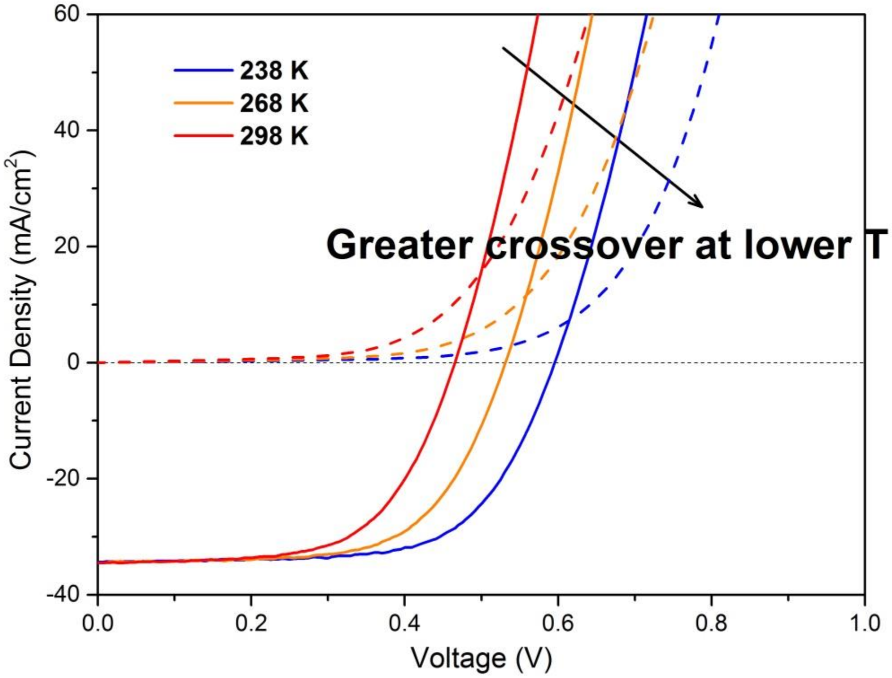

Figure 4.11 Experimental CIGS J-V curves with varying temperature

Fig. 4.12 shows the conduction bands and quasi-Fermi levels of the same cell operating at three different temperatures and Fig. 4.13 shows the calculated J-V characteristics. In Fig.

4.12(a), although the secondary barrier varies little with the temperature ($\phi \sim 0.46\ eV$) for all three temperatures, the secondary barrier at low temperatures will increasingly limit the electron current (Section 3.2). At T = 238 K in the dark, for example, the secondary barrier ($\phi = 0.46\ eV$) is greater than the maximum distortion-free secondary barrier $\phi_{max} = 0.358\ eV$, which indicates that the electron current across the interface will be limited at a greater degree than when the J-V dark curve is measured at T = 298 K. Under this condition, the cell will sacrifice more voltage to achieve the same amount forward current as the high temperature case in dark, and a right shift of the dark J-V curve takes place. Under illumination, the barriers for all the three temperatures are smaller than their corresponding maximum distortion-free secondary barriers ϕ_{max}, and there is little effect on the electron current flowing through the interface. Although the right shift of light J-V curve at low temperature can offset part of the J-V crossover, the greater right shift of dark J-V curve still dominates. Therefore, greater J-V crossover is observed at lower temperature.

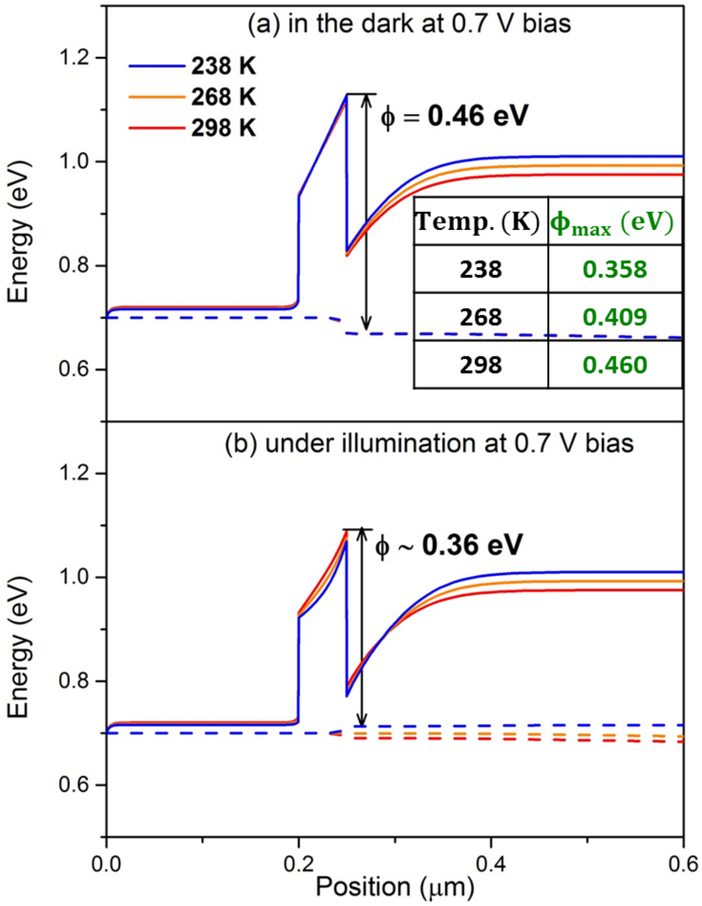

Figure 4.12 Simulated band diagrams with different operation temperature: (a) in the dark at 0.7 V bias, and (b) under illumination at 0.7 V bias.

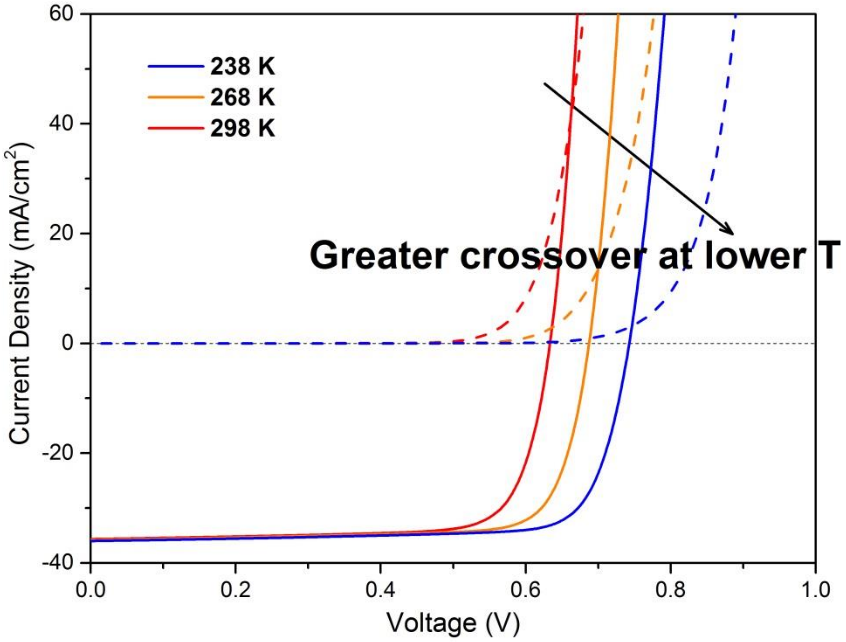

Figure 4.13 Simulated J-V curves for different operating temperatures

4.2 J-V Distortion – Red Kink

Section 3.3.2 discussed how the secondary barrier at the buffer-absorber interface can lead to a kink in the J-V curve under illumination with red light. The thermionic current J_{TE} we have introduced to illustrate the J-V red kink in Section 3.3.2 varies with the barrier height. As discussed in Section 3.2 the conduction-band offset at the interface and the doping density in Zn(O,S) can influence the barrier height at the interface. In addition, the trapped electrons in Zn(O,S) will be released from deep-level defects due to the photoconductivity and thus reduce the barrier height when at least some of the photons have energy greater than the band bap of the Zn(O,S) buffer (Section 3.2).

Experimentally, the J-V red kinks varies with different recipes, such as varying oxygen fraction in the sputter beam and substitution of non-In-doped ZnS target with In-doped ZnS target. The device-physics question is how to relate these experimental J-V red kinks to CBO and doping density. Numerical simulation allows us to investigate the J-V red kinks with varying oxygen fraction in the sputter beam and In-doped or not in Section 4.2.1 and 4.2.2, respectively. In Section 4.2.3, the effect of blue photon exposure time on the elimination of the J-V red kink will be discussed.

4.2.1 Effect of Oxygen on Red Kink

The J-V red kink under red-light illumination, is particularly pronounced when there is a low oxygen fraction in the sputter beam. Fig. 4.14 shows that, the lower the oxygen fraction in the Zn(O,S) sputtering process, the larger J-V red kink observed. Under blue or white light illumination, there is little kink in the corresponding J-V curves except for the lowest oxygen fraction (0.60% O_2) case shown.

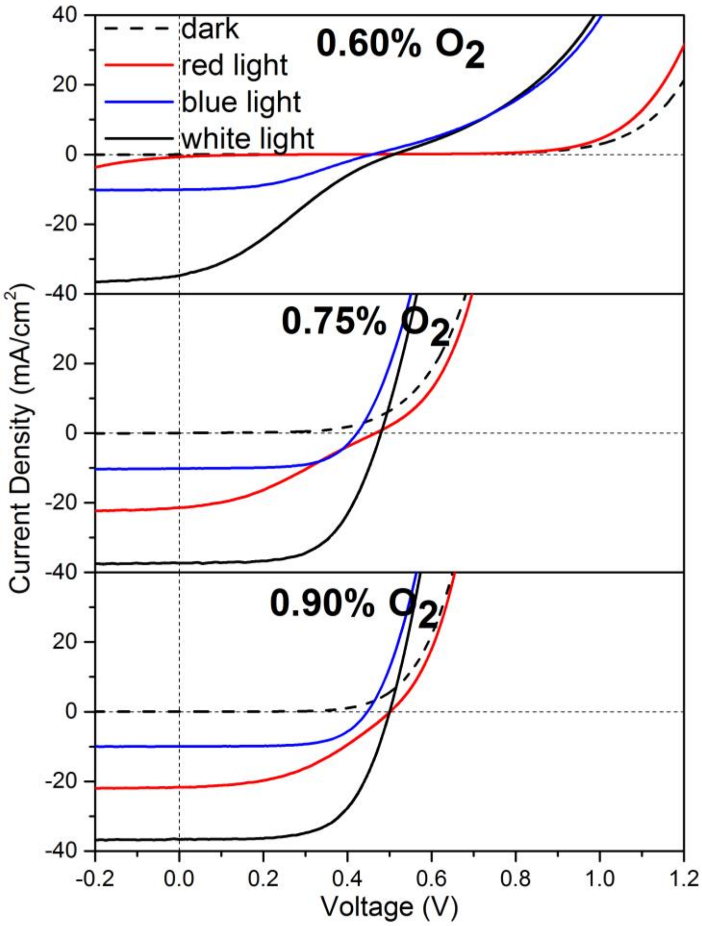

Figure 4.14 Experimental J-V red kinks at a variety of oxygen fraction in the sputter beam

In Section 4.1.1, we have concluded that the conduction-band offset (CBO) at the interface is varied with the oxygen content in Zn(O,S) and a greater J-V crossover with an increasing amount of oxygen content in the Zn(O,S) films is due to the increase of CBO- induced barrier height. Numerical simulation is employed here to test whether the red kink is also a consequence of the CBO-induced barrier.

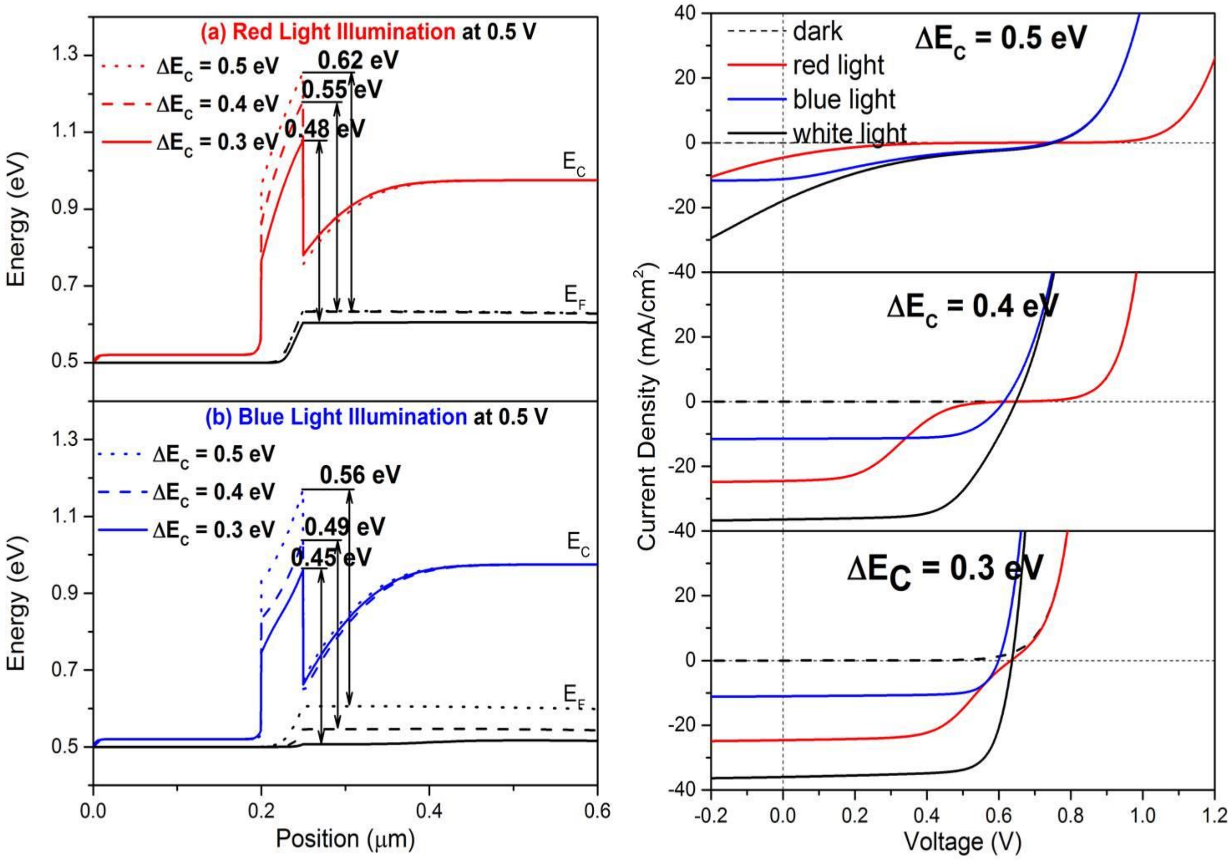

Figure 4.15 (Left) simulated band diagram for for a variety of CBO - ΔE_C at 0.5 V bias: (a) under red-light illumination, and (b) under blue-light illumination; (right) the corresponding simulated J-V curves

Comparison of (a) and (b) in Fig. 4.15 shows that the heights of all the secondary barriers under blue-light illumination are greater than those under red-light illumination. This phenomenon can be explained as follows: due to the photoconductivity of Zn(O,S) (Section 3.2), electrons trapped in the deep-level defects will be released when exposed to blue photons whose energy is larger than $E_{g(Zn(O,S))}$. As a result, the additional free electrons in the Zn(O,S) buffer under blue-light illumination will reduce the barrier height to a level that it is favorable for electrons current to flow across the barrier. Thus, the blue-light J-V curves are much better well-shaped than the red-light curves. More importantly, the J-V curve under red-light illumination becomes less kinked with smaller conduction-band offset. In the band diagram (a) of Fig. 4.15, under red-light illumination at 0.5 V bias, the barriers for all the ΔE_C cases are higher than 0.46 eV, which limits the thermionic current J_{TE} but to varying degrees – the greater the barrier height is the more seriously J_{TE} is limited. In the band diagram (b) of Fig. 4.15, under blue-light illumination at 0.5 V bias, the barriers for all the ΔE_C cases are reduced to varying degrees compared to the corresponding barriers under red-light illumination, due to the photoconductivity of Zn(O,S). The blue-light J-V curves are well shaped except for the $\Delta E_C = 0.5\ eV$ case where a high barrier still exists. Note that, the larger step in the quasi-Fermi levels under red-light illumination increasingly helps the photo-generated electron current $J_{ph}(< 0)$ flow from right to left. In other words, it is easier to achieve the same net current as for blue-light J-V curve, which explains the presence of the J-V red kink. Comparison of Fig. 4.14 and 4.15 (right) shows that the calculated red kink trend is qualitatively consistent with experiment, which strongly suggests that the J-V red kink with less oxygen fraction in the sputter beam is closely related to the CBO-induced barrier at the buffer-absorber interface.

4.2.2 Effect of Zn(O,S) doping on Red Kink

In Section 4.1.2, we found that the J-V crossover is strongly dependent on the indium doping in the Zn(O,S) buffer layer. Similarly, the J-V red kink was also observed to have a strong dependence on indium doping, as seen in Fig. 4.16. The Zn(O,S) buffer layers in the two cells are both sputtered at the same conditions (0.7% O_2 in the argon beam with substrate temperature 200 ℃), except for different ZnS targets (with and without In doping).

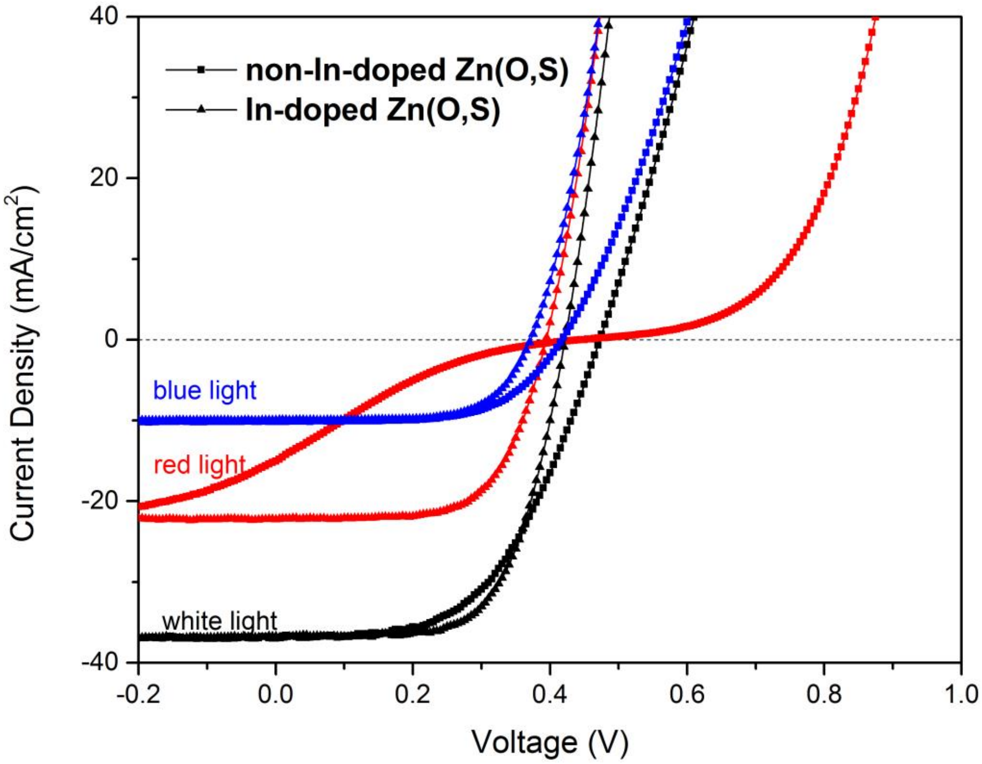

Figure 4.16 Experimental J-V red kink of CIGS cells with In-doped and non-In-doped Zn(O,S)

Note that the barrier height at the buffer-absorber interface, which can be modulated by the free electron density in the buffer layer (Section 3.2), is responsible for the formation of J-V red kink (Section 3.3.2). In addition, due to the photoconductivity of Zn(O,S), the free electron density in the Zn(O,S) buffer will be smaller under red-light illumination than with blue or white-light illumination. One may thus hypothesize that the J-V red kink difference between the In-doped and non-In-doped Zn(O,S) buffer is due to the variation of the free electron density ($n_{Zn(O,S)}$) in Zn(O,S). To verify such hypothesis, the numerical simulation is again employed.

In the simulation, we set the same CBOs ($\Delta E_C = 0.4\, eV$) for both $n_{Zn(O,S)} = 5 * 10^{16} cm^{-3}$ and $n_{Zn(O,S)} = 5 * 10^{17} cm^{-3}$. All the other simulation parameters are from the baseline Table 2-1. Fig. 4.17 shows the simulated band diagrams for these two different $n_{Zn(O,S)}$ cases at 0.5 V bias.

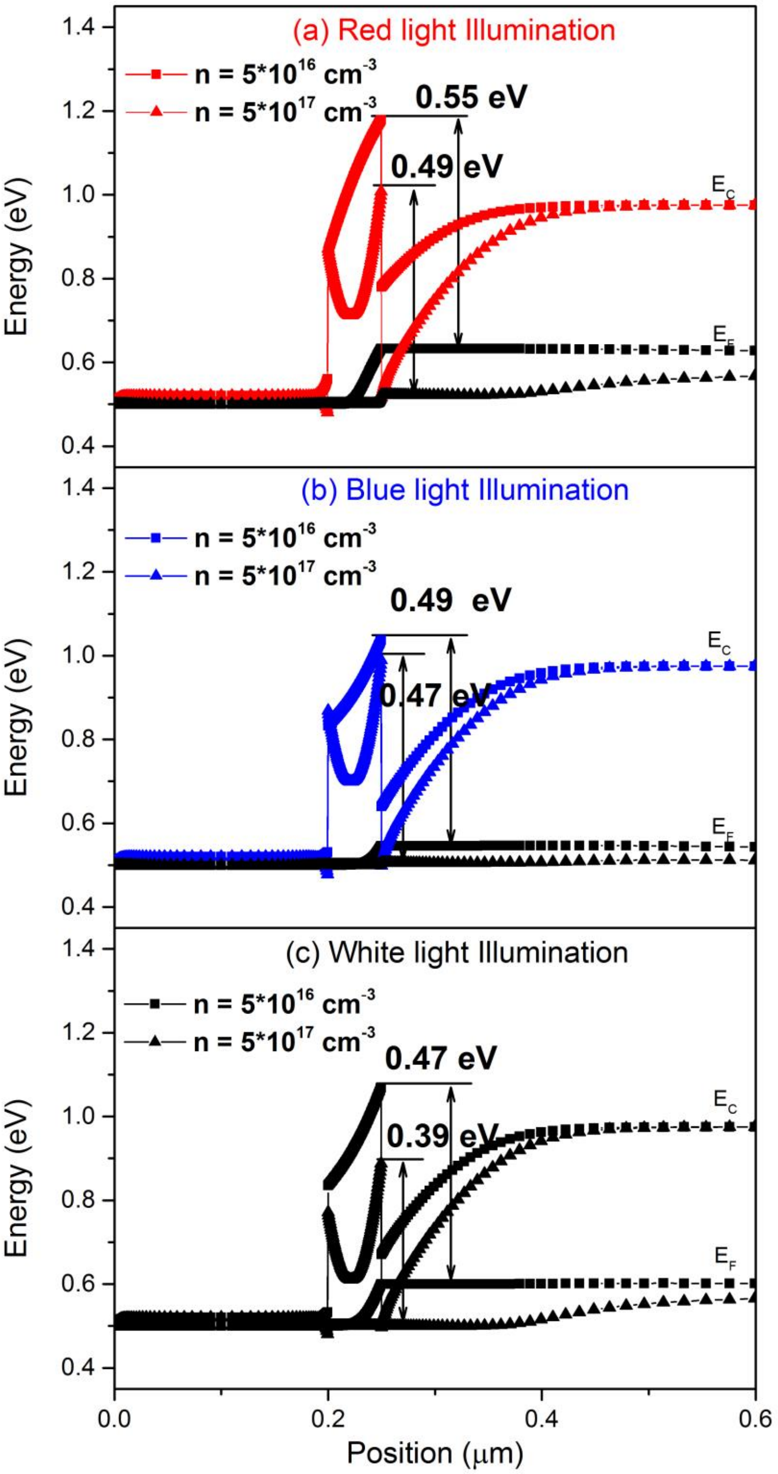

Figure 4.17 Simulated band diagram for two $n_{Zn(O,S)}$ cases at 0.5 V bias: (a) under red-light illumination, (b) under blue-light illumination, and (c) under white-light illumination.

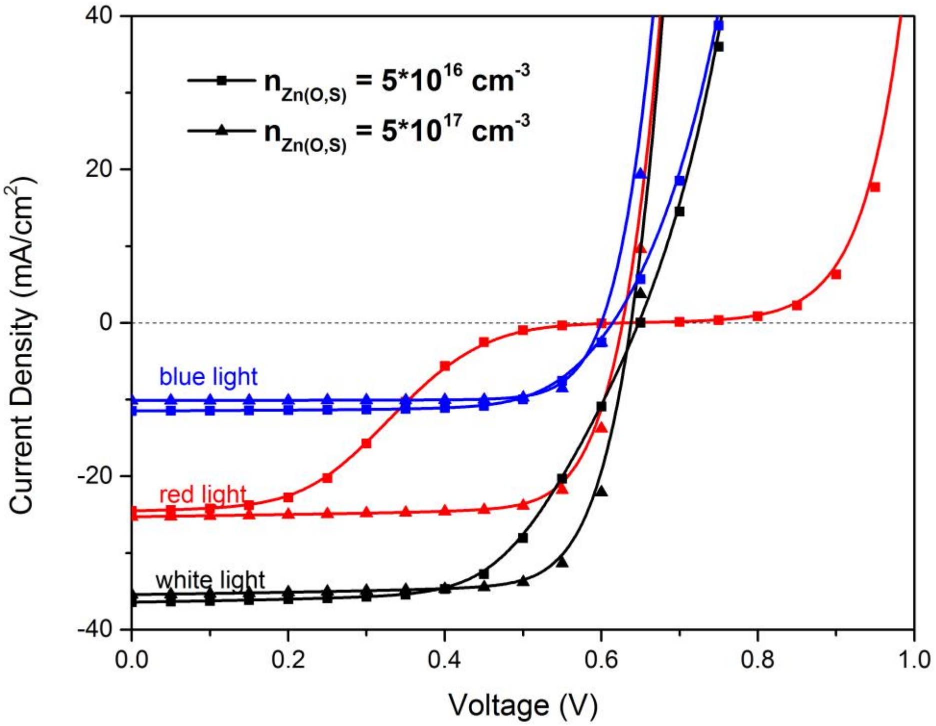

Figure 4.18 Simulated J-V curves for two $n_{Zn(O,S)}$ cases under different illumination conditions

In Fig. 4.17(a), under red-light illumination, most of the trapped free electrons cannot be released from the deep-level defects by the red photons with the energy $h\nu < E_{g(Zn(O,S))}$. The low doping density ($n_{Zn(O,S)} = 5 * 10^{16} cm^{-3}$) is comparable with the deep-level defect density in Zn(O,S) ($N_{AG} = 1 * 10^{17} cm^{-3}$), thus most of the free electrons in Zn(O,S) will be trapped, which leads to a low free electron density and higher barrier at the interface ($\phi = 0.55\ eV$); the higher doping density ($n_{Zn(O,S)} = 5 * 10^{17} cm^{-3}$), however, is greater than the deep-level defect density, and thus the trapped electrons have a smaller effect on the total amount of free electrons which leads to a lower barrier at the interface ($\phi = 0.49\ eV$). As a result, in Fig. 4.18, the simulated red-light J-V curve for $n_{Zn(O,S)} = 5 * 10^{16} cm^{-3}$ is much more seriously kinked than that for $n_{Zn(O,S)} = 5 * 10^{17} cm^{-3}$. In Fig. 4.17(b), under blue-light illumination, however, most of the trapped electrons for both cases will be released with the help of the high energy photons, which leads to a reduced barrier height at the interface. The blue-light case shown has a smaller photocurrent so presumably can tolerate a higher barrier. Therefore, both of their blue-light J-V curves are little kinked in Fig. 4.18 event though their barriers are slightly higher than $\phi_{max} = 0.46\, eV$ at T = 298 K. In Fig. 4.17(c), under white-light illumination, again due to the photoconductivity of Zn(O,S) and larger amount of photons the secondary barriers for both doping densities continuously decrease. Their light J-V curves are well-behaved in Fig. 4.18. Comparing the simulated J-V curves in Fig. 4.18 with the experimental J-V curves in Fig. 4.17, a similar J-V characteristic trend are observed: high doping density in Zn(O,S) (In-doped) has a better-shaped J-V curves for all the three illumination conditions; under red-light illumination, the red kink only exists in the low doping Zn(O,S) (non-In-doped). Therefore, it is suggested that the low doping density in Zn(O,S) is responsible for the J-V red kink for the CIGS cells with non-In-doped Zn(O,S) buffer layer.

4.2.3 Impact of Blue-Photon Exposure Time

Fig. 4.19(a) shows the initial red light J-V as a function of white-light exposure time for a cell with sputter Zn(O,S) buffer at 0.4% oxygen fraction without In doping. The red-light curve prior to any white-light exposure was the most distorted. The curves gradually shifted towards the well-behaved light J-V curve with increasing time of white-light exposure. The red-light curves measured after 2-hr exposure, however, are still heavily distorted and did not quite match up with the well-behaved white-light curve. Fig. 4.19(b) shows a series of red-light curves measured as a function of the elapsed time in the dark following the white-light exposure. The red-light J-V curve returns to a larger red kink with increased elapsed time, but at a slow rate. The J-V transition rates (both the red-kink removal after white-light exposure and relaxation in the dark) in sputtered Zn(O,S)/CIGS cell are significantly slower than those reported for CBD

CdS/CIS and InS(O,OH)/CIGS cells [15]. Note that the band gaps of CBD CdS and InS(O,OH) in [15] are approximately 2.4 eV, and 2.8 eV, respectively. However, the sputtered Zn(O,S) buffer we are investigating here has a greater band gap, about 3.0 eV. Therefore, the slower J-V response after white-light exposure of sputtered Zn(O,S)/CIGS cells can be explained, at least partly, by the smaller amount of photons per unit of time absorbed in the wider band-gap buffer from the same white light spectrum. Thus slower kink removal would result from a smaller photon fluxes; the slower J-V relaxation in the dark may be due to a similarly slower electron-capture rate in the buffer. To help understand the details, quantitative analysis on the experimental J-V transition rates will be discussed in Section 4.3.3.

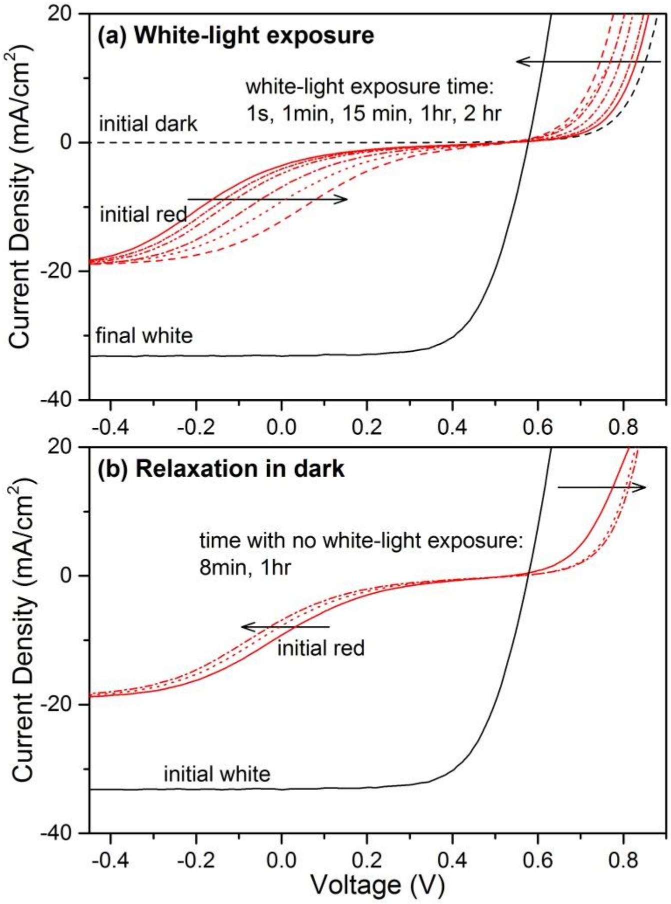

Figure 4.19 Experimental J-V curves from a Zn(O,S)-CIGS cell: (a) Transition from seriously distorted to less distorted experimental curves with white-light exposure; (b) reverse transition in the dark

4.3 Quantitative Comparison of J-V Distortion

In the previous discussions in Section 4.1 and 4.2, the physical mechanisms of various J-V distortion cases were investigated by the comparative analysis of experimental and simulated J-V characteristics. Quantification of J-V distortion, however, which can help explicitly relate the physical explanation of J-V distortion to change in experimental parameters, is done in this section. Note that the quantitative J-V distortion comparison for varying doping density case will not be discussed in the following sections due to a lack of specific indium-doping profile in experiment.

4.3.1 Definition of Distortion-related Parameters

Several characteristic features among the dark, red-light, and white-light J-V curves for a typical sputtered Zn(O,S)/CIGS cell are seen in Fig. 4.20. The dark J-V curve has a higher turn-on voltage compared to the well-behaved white light curve due to the reduced barrier caused by the photoconductivity of Zn(O,S) under standard AM1.5 white light illumination. The J-V crossover between the dark and white-light curves is quite pronounced. The red-light curve has a low-bias region with well-behaved collection, a mid-bias region with decreasing collection, and a high-bias region where the curve merges with the dark curve. To quantify these characteristic features of J-V distortion, it is helpful to define the following terms in the corresponding J-V curves [31].

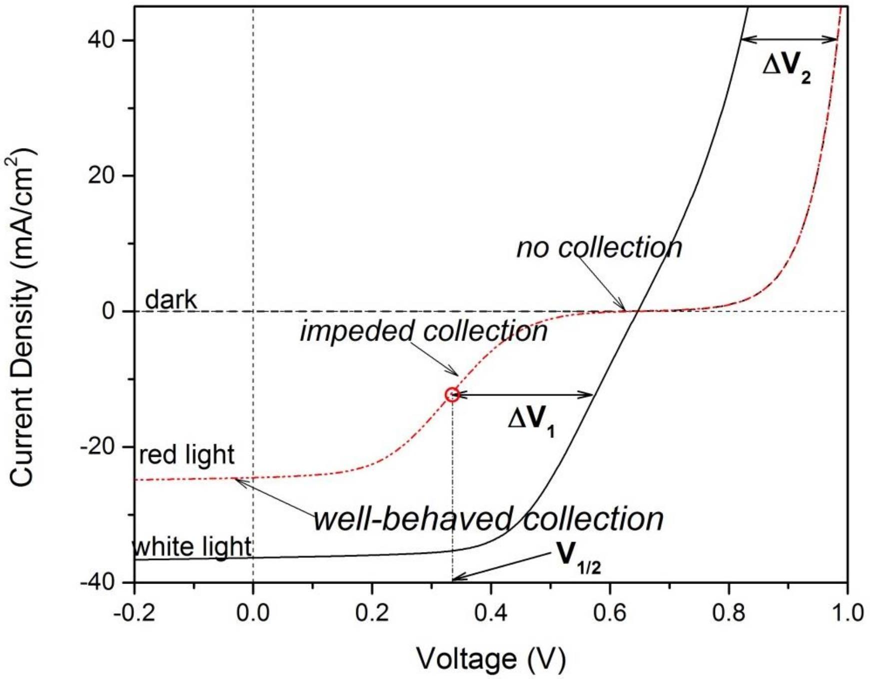

Figure 4.20 Quantitative J-V distortions with kink parameters $V_{1/2}$, ΔV_1, and ΔV_2

- $V_{1/2}$: is the voltage at half-maximum photon-generated current under red light illumination, related to the red kink distortion.
- ΔV_1: is the red-white collection voltage difference at half-maximum photon-generated current under red light illumination, related to the red kink distortion as well.
- ΔV_2: is the dark-white non-superposition at forward current $J = 40\ mA/cm^2$, related to the crossover between dark and light J-V curves.

4.3.2 Correlation of J-V distortion between CBO and O_2% in Zn(O,S)

In Section 4.1.1 and 4.2.1, we have concluded that the J-V distortion (crossover and red kink) varying with the oxygen content in the Zn(O,S) buffer is related to the CBO at the buffer-absorber interface. The distortion comparisons between experiment and simulation (Fig. 4.2 vs.

Fig. 4.4 for crossover, Fig. 4.14 vs. Fig. 4.15 for red kink), however, are qualitative, and here it will be made more quantitative.

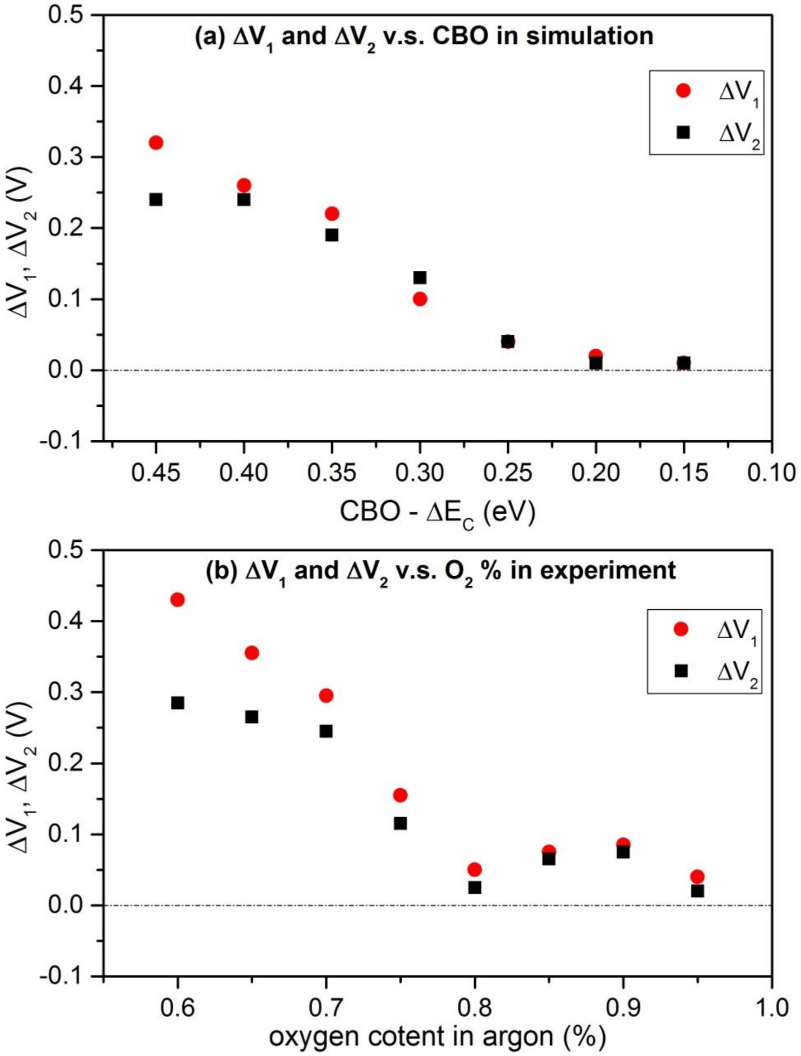

Figure 4.21 Quantitative correlation between simulated and experimental J-V distortions: (a) ΔV_1 and ΔV_2 v.s. CBO in simulation; and (b) ΔV_1 and ΔV_2 v.s. $O_2\%$ in experiment.

Fig. 4.21(a) shows a strong CBO dependence on both the J-V red kink (ΔV_1) and crossover (ΔV_2) in simulation. In fact, ΔV_1 and ΔV_2 are nearly equal. With decreased CBO at the buffer-absorber interface, the reduced secondary barrier will allow more electron current to flow with less consumption of voltage and thus lead to a better-shaped J-V curve (the photoconductivity helps to eliminate the red-kink distortion as well); when CBO is low enough (<0.3 eV), the J-V curves are well-behaved. Fig. 4.21(b) shows a strong $O_2\%$ dependence on the

J-V distortion in experiment: greater J-V red kink and crossover appear in the low oxygen content region. As the oxygen content in Zn(O,S) is increased, the increased conduction band edge of Zn(O,S) [27] lowers the secondary barrier at the interface and thus contribute to a smaller J-V distortion; at high oxygen content (0.8-1.0% O_2), there is little J-V distortion in sputtered Zn(O,S)/CIGS cells. The experimental data is not as smooth as the simulation, but the trend is clear, and again there is similarity between ΔV_1 and ΔV_2. The fact that J-V distortion trend as a function of CBO in simulation is consistent with the J-V distortion trend as a function of O_2% in experiment, allows one to credibly relate the CBO and J-V distortion directly to the oxygen fraction in the sputter beam.

4.3.3 Dependence of Light-intensity and Temperature

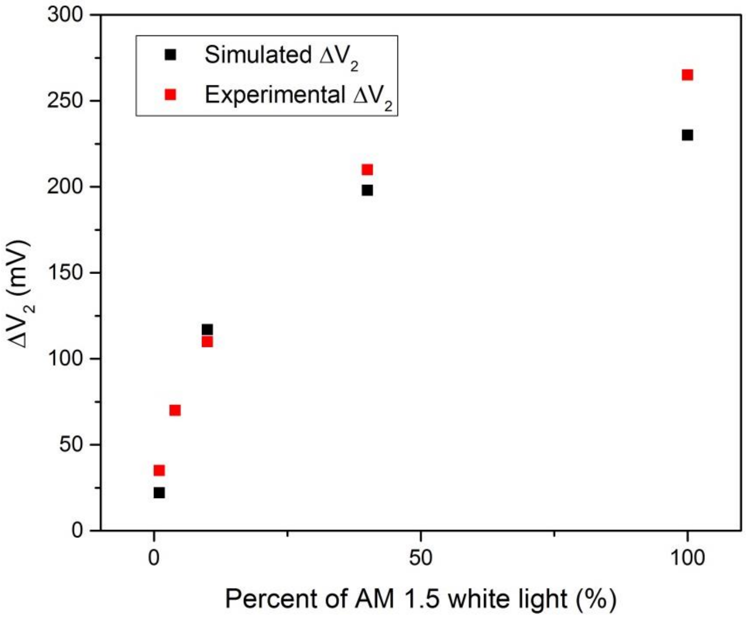

Figure 4.22 Quantitative light-intensity dependent J-V distortion: Simulated ΔV_2 v.s. experimental ΔV_2

In Section 4.1.3, we have concluded that the smaller the light intensity is, the smaller the J-V crossover between dark and light curves. In other words, the lower light-intensity illumination will push the corresponding J-V curve right towards to the dark J-V curve at high bias due to a higher secondary barrier at the interface and thus a greater consumption of voltage drop across the buffer. Fig. 4.22 shows a quantitative comparison of light-intensity dependent J-V crossover (ΔV_2) obtained from a simulated Zn(O,S)/CIGS cell with $\Delta E_C = 0.4\ eV$ and an experimental Zn(O,S)/CIGS cell with 0.65% O_2 in argon gas. The simulated and experimental data points hold the same J-V crossover increasing trend with smaller light intensity. In addition, the simulated ΔV_2 in each light-intensity case is in good agreement with the corresponding experimental ΔV_2, again indicating the credibility of our theoretical diode model.

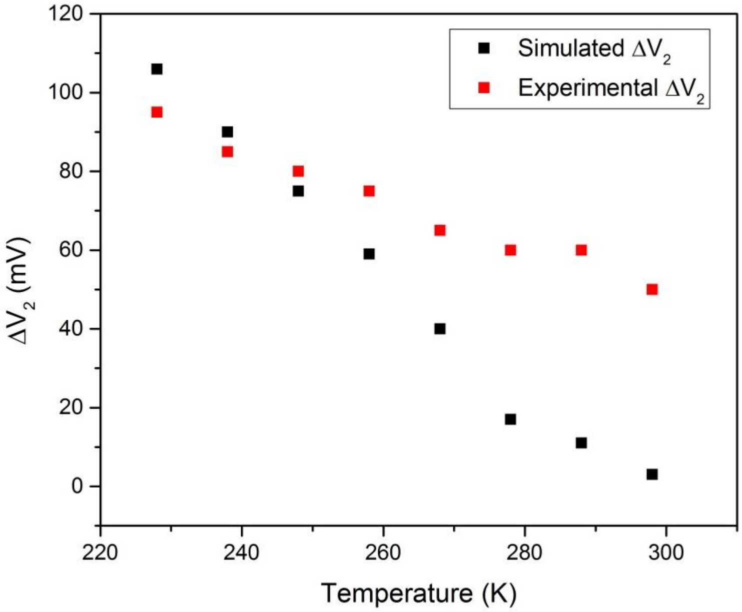

Figure 4.23 Quantitative temperature dependent J-V distortion: Simulated ΔV_2 v.s. experimental ΔV_2

In addition to light intensity, the operating temperature has an effect on the J-V crossover: the lower the operation temperature, the greater the J-V crossover. Same barrier allows less current at lower temperatures. Fig. 4.23 shows a quantitative comparison of temperature-dependent crossover obtained from a simulated Zn(O,S)/CIGS cell with $\Delta E_C = 0.3\ eV$ and an experimental Zn(O,S)/CIGS cell with 0.85% O_2 in argon gas. In both simulation and experiment, the J-V crossover shows a decreasing trend at higher temperature. In the high temperature range (278-298 K), however, there is a greater amount of crossover in experiment than in simulation. Perhaps, the defect density of Zn(O,S) [16] or other undetermined factors will contribute to such high J-V crossover as well. More comprehensive investigation would be needed here.

4.3.4 Blue-photon-enhanced Recovery of Red-light J-V

Fig. 4.24 shows the characteristic voltage for the red-kink J-V curve versus white-light exposure time. The curves gradually shifted towards the well-behaved light J-V curve with increasing time of white-light exposure. The key parameter $V_{1/2}$ starts out negative, and should with time approach V_{OC}. After 2-hour white light exposure, however, the red-light J-V curve is still heavily distorted. The removal rate of red kink in sputtered Zn(O,S)/CIGS cell are significantly slower compared to the results in CBD CdS/CIS and InS(O,OH)/CIGS cells (Fig. 4.25) [15]. Partly, it can be explained by the fact that a wider band gap of Zn(O,S) buffer limits the amount of photons per unit of time absorbed in the buffer, and thus fewer free electrons will be released from the deep-level defect state and higher barrier is formed to lower the rate to remove J-V red kink.

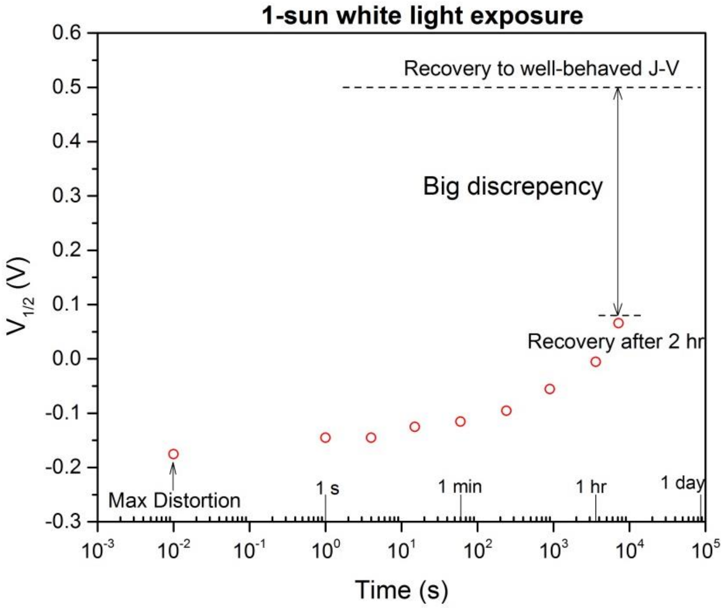

Figure 4.24 Red kink parameter $V_{1/2}$ vs. time of white-light exposure for a Zn(O,S)/CIGS cell with 0.4% O_2 in argon gas

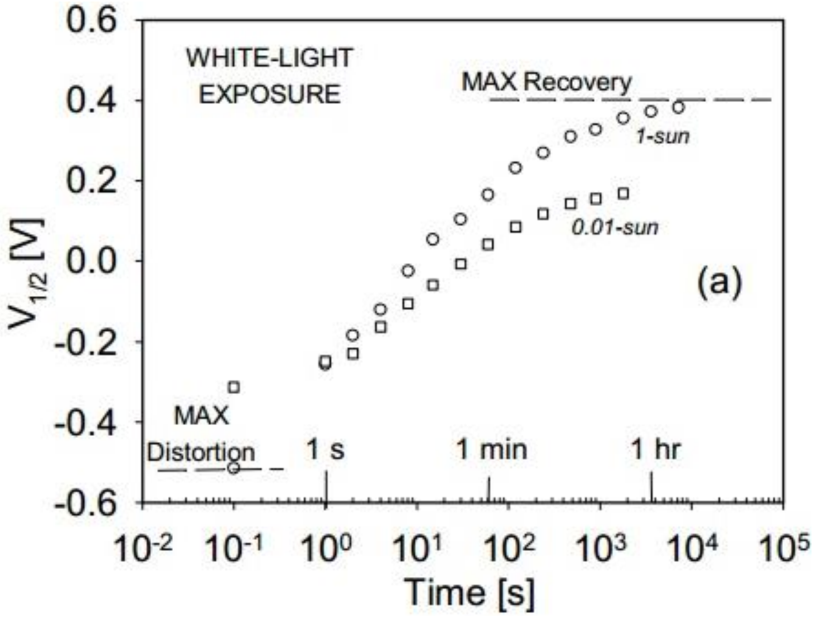

Figure 4.25 Red kink parameter $V_{1/2}$ vs. time of white-light exposure for a CBD CdS/CIS cell from Pudov [15]

Chapter 5

Conclusions

In this thesis, the experimental J-V distortion (including both red kink and crossover) of CIGS solar cells with a sputtered Zn(O,S) window layer and its physical explanation were described with a straightforward photodiode model that was extended under different Zn(O,S) recipes and various J-V measurement conditions. It was shown that the secondary barrier at the buffer-absorber interface which is influenced by both the internal material properties, such as the conduction-band offset (CBO) at the interface and the doping density of the buffer layer, and the external effects such as the light-intensity and operating temperature, plays a crucial role in the current-transport mechanisms and thus governing J-V distortion. The quantitative comparison of J-V distortion between simulation and experiment was employed to examine the credibility of the secondary barrier theory.

The CBO-induced J-V distortion was verified through examination of CIGS solar cells with various oxygen fractions in the sputtered Zn(O,S) buffer layer. In the experimental data, the J-V distortion varies with oxygen fraction in Zn(O,S): more distortion with less oxygen. With a varying amount of oxygen fraction in Zn(O,S), the electron affinity of Zn(O,S) will be modulated and thus leads to the change of CBO at the buffer-absorber interface. Comparing the data with the numerical J-V characteristics, we found that such a CBO-induced barrier at the buffer-absorber interface which limits the electron current flowing through is responsible for the distortion. In addition, the doping density in the buffer layer is directly related to the secondary barrier. With the increased doping density of Zn(O,S), the reduced barrier height results in a less current limitation and thus a smaller J-V crossover and red kink. The In-doped Zn(O,S)/CIGS cell with a higher doping density has better-behaved experimental J-V curves than the non-indium-doped Zn(O,S)/CIGS cell's, which is in good agreement with the numerical simulation.

The external effects, such as the operating temperature and light intensity, also contribute to modulate J-V distortion. Both experimental and simulated J-V results show that, at lower temperature, there is a greater J-V crossover between dark and light J-V curves. Such temperature-dependent J-V distortion can be explained by the temperature-dependent secondary barrier: with decreased temperature, the maximum distortion-free barrier ϕ_{max} that allows full electron current to flow through the interface is reduced and results in a more serious current limitation, indicating a greater J-V crossover between dark and light curves. In addition, it is observed that the J-V crossover varies with the light intensity: the smaller the light intensity one applies to, the closer the corresponding J-V curve is to the dark J-V for forward currents. Under lower light-intensity illumination, there is a smaller fraction of photons with $h\nu > E_{g(Zn(O,S)}$ which can excite the buffer layer to release the trapped electrons from the deep-level defect state. The result is a lower doping density of Zn(O,S) and thus a greater secondary barrier to limit the electron current through the interface. In other words, the lower light-intensity will push the corresponding J-V curve to the right towards the dark J-V curve at high bias ($V > V_{OC}$), and thus less J-V crossover takes place. It is also found that the blue-photon flux can partially mitigate the red-kink distortion but does not match the well-behaved white light J-V curve. This find observation can be partly explained by a lower amount of photons per unit of time absorbed in wider band-gap Zn(O,S) buffer from the same white light spectrum, and thus slower kink removal due to its photoconductivity.

Bibliography

1. *World Energy Consumption from Wikipedia*. Available from: http://en.wikipedia.org/wiki/World_energy_consumption.
2. EPIA. *Global Market Outlook For Photovoltaics 2013-2017*. 2013; Available from: http://www.epia.org/fileadmin/user_upload/Publications/GMO_2013_-_Final_PDF.pdf.
3. Reuters. *Germany sets new solar power record, institute says*. 2012; Available from: http://www.reuters.com/article/2012/05/26/us-climate-germany-solar-idUSBRE84P0FI20120526.
4. OpenEI. *Transparent Cost Database*. Available from: http://en.openei.org/apps/TCDB/.
5. Wolden, C.A., et al., *Photovoltaic manufacturing: Present status, future prospects, and research needs.* Journal of Vacuum Science & Technology A: Vacuum, Surfaces, and Films, 2011. **29**(3): p. 030801-030801-16.
6. IEA. *Technology Roadmap: Solar photovoltaic energy*. 2010; Available from: http://www.iea.org/publications/freepublications/publication/pv_roadmap.pdf.
7. Jackson, P., et al., *New world record efficiency for Cu (In, Ga) Se2 thin‐film solar cells beyond 20%.* Progress in Photovoltaics: Research and Applications, 2011. **19**(7): p. 894-897.
8. *Solar Frontier Sets New Efficiency World Record*. 2012; Available from: http://www.solar-frontier.com/eng/news/2012/C002980.html.
9. *Japan's Largest Solar Panel Factory Reaches Full Commercial Operations, Announces Solar Frontier*. 2011; Available from: http://www.solar-frontier.com/eng/news/2011/C002132.html.
10. *TSMC Solar – best-in-class production of groundbreaking products*. Available from: http://www.tsmc-solar.com/technology/production.
11. *CIGS PV firm MiaSolé raises a further $55m from VC investors*. 2012; Available from: http://www.semiconductor-today.com/news_items/2012/MAR/MIASOLE_080312.html.
12. Gloeckler, M., *Ph.D thesis - DEVICE PHYSICS OF Cu(In,Ga)Se2 THIN-FILM SOLAR CELLS*, in *Department of Physics*. 2005, Colorado State University.
13. Sharbati, S. and J. Sites, *Impact of the band offset for n-Zn(S,O)/p-Cu(In,Ga)Se2 solar cells.* to be published.
14. Ramanathan, K., et al. *A comparative study of Zn (O, S) buffer layers and CIGS solar cells fabricated by CBD, ALD, and sputtering*. in *Photovoltaic Specialists Conference (PVSC), 2012 38th IEEE*. 2012. IEEE.

15. Pudov, A., *Ph.D thesis - IMPACT OF SECONDARY BARRIERS ON CuIn1−xGaxSe2 SOLAR-CELL OPERATION*, in *Department of Physics*. 2005, Colorado State University.

16. Kanevce, A., et al. *Conduction-band-offset rule governing JV distortion in CdS/CI (G) S solar cells*. in *MRS Proceedings*. 2005. Cambridge Univ Press.

17. Contreras, M.A., et al., *SHORT COMMUNICATION: ACCELERATED PUBLICATION: Diode characteristics in state‐of‐the‐art ZnO/CdS/Cu (In1− xGax) Se2 solar cells.* Progress in Photovoltaics: Research and Applications, 2005. **13**(3): p. 209-216.

18. Naghavi, N., et al., *Buffer layers and transparent conducting oxides for chalcopyrite Cu (In, Ga)(S, Se) 2 based thin film photovoltaics: present status and current developments.* Progress in Photovoltaics: Research and Applications, 2010. **18**(6): p. 411-433.

19. Y. Liu, Y.S., and A. Rockett. *wxAMPS Simulation software*. Available from: https://wiki.engr.illinois.edu/display/solarcellsim/Simulation+Software.

20. Fonash, S. *AMPS-1D*. 2010; Available from: http://www.ampsmodeling.org/.

21. Liu, Y., Y. Sun, and A. Rockett, *A new simulation software of solar cells—wxAMPS.* Solar Energy Materials and Solar Cells, 2012. **98**: p. 124-128.

22. Gloeckler, M., A. Fahrenbruch, and J. Sites. *Numerical modeling of CIGS and CdTe solar cells: setting the baseline*. in *Photovoltaic Energy Conversion, 2003. Proceedings of 3rd World Conference on*. 2003. IEEE.

23. Sze, S.M. and K.K. Ng, *Physics of semiconductor devices*. 2006: Wiley. com.

24. Horio, K. and H. Yanai, *Numerical modeling of heterojunctions including the thermionic emission mechanism at the heterojunction interface.* Electron Devices, IEEE Transactions on, 1990. **37**(4): p. 1093-1098.

25. Durbin, S.M. and J. Gray. *Considerations for modeling heterojunction transport in solar cells*. in *Photovoltaic Energy Conversion, 1994., Conference Record of the Twenty Fourth. IEEE Photovoltaic Specialists Conference-1994, 1994 IEEE First World Conference on*. 1994. IEEE.

26. Yang, K., J.R. East, and G.I. Haddad, *Numerical modeling of abrupt heterojunctions using a thermionic-field emission boundary condition.* Solid-State Electronics, 1993. **36**(3): p. 321-330.

27. Persson, C., et al., *Strong Valence-Band Offset Bowing of ZnO_ {1-x} S_ {x} Enhances p-Type Nitrogen Doping of ZnO-like Alloys.* Physical review letters, 2006. **97**(14): p. 146403.

28. Bube, R.H. and E.L. Lind, *Photoconductivity of Zinc Selenide Crystals and a Correlation of Donor and Acceptor Levels in II-VI Photoconductors.* Physical Review, 1958. **110**(5): p. 1040.

29. Orton, J., et al., *The mechanism of photoconductivity in polycrystalline cadmium sulphide layers.* Journal of Applied Physics, 1982. **53**(3): p. 1602-1614.

30. Eisgruber, I., et al., *Blue-photon modification of nonstandard diode barrier in CuInSe< sub> 2</sub> solar cells.* Solar Energy Materials and Solar Cells, 1998. **53**(3): p. 367-377.

31. Pudov, A., et al., *Secondary barriers in CdS–CuIn 1-x Ga x Se 2 solar cells.* Journal of applied physics, 2005. **97**(6): p. 064901-064901-6.

32. *Reference Solar Spectral Irradiance: Air Mass 1.5*. Available from: http://rredc.nrel.gov/solar/spectra/am1.5/#about.

33. Grimm, A., et al., *Junction formation in chalcopyrite solar cells by sputtered wide gap compound semiconductors.* Thin Solid Films, 2011. **520**(4): p. 1330-1333.

34. Benouis, C., et al., *The effect of indium doping on structural, electrical conductivity, photoconductivity and density of states properties of ZnO films.* Journal of Alloys and Compounds, 2010. **490**(1): p. 62-67.